EUROPEAN LABORATORY FOR PARTICLE PHYSICS

Status report to the proposal SPSC-P-330

Report from the NA61/SHINE experiment at the CERN SPS

By the NA61/SHINE Collaboration

http://na61.web.cern.ch/

CERN-SPSC-2015-036 / SPSC-SR-171
14/10/2015

Abstract

This document reports on the status and plans of the NA61/SHINE experiment at the CERN SPS as of October 2015. First, an overview of the 2014 and 2015 data-taking period on p+Pb interactions at 158 GeV/c and Ar+Sc collisions at 13A GeV/c–150A GeV/c is given. The latter data-taking with the first primary Ar beams at CERN was a major success. Second, the facility maintenance and upgrades are briefly presented. The VTX-1 magnet was damaged at the beginning of the 2015 proton period. The physics data-taking for p+p interactions at 400 GeV/c and for the Fermilab neutrino beams as well as the pilot data taking on Pb+Pb collisions at 30A GeV/c was replaced by detector tests and calibration runs. Third, the advance in the NA61/SHINE software and calibration procedures is briefly reported. Fourth, new physics results are presented. In particular, the very first results on Ar+Sc collisions are presented. Fifth, plans for data taking in 2016–2018 are outlined and ideas concerning the NA61/SHINE physics programme beyond 2020 are sketched.

The proposal for the beam momentum scan with Pb+Pb interactions is presented in a separate addendum document submitted in parallel to this Status Report.

October 14, 2015

Contents

The NA61/SHINE Collaboration

A. Aduszkiewicz[15], Y. Ali[13], E. Andronov[21], T. Antićić[2], N. Antoniou[7], B. Baatar[19], F. Bay[23], A. Blondel[25], J. Blümer[4], M. Bogomilov[1], A. Brandin[20], A. Bravar[25], J. Brzychczyk[13], S.A. Bunyatov[19], O. Busygina[18], P. Christakoglou[7], M. Ćirković[22], T. Czopowicz[17], N. Davis[7], S. Debieux[25], H. Dembinski[4], M. Deveaux[6], F. Diakonos[7], S. Di Luise[23], W. Dominik[15], T. Drozhzhova[21], J. Dumarchez[3], K. Dynowski[17], R. Engel[4], A. Ereditato[24], G.A. Feofilov[21], Z. Fodor[8,16], A. Garibov[0], M. Gaździcki[6,11], M. Golubeva[18], K. Grebieszkow[17], A. Grzeszczuk[14], F. Guber[18], A. Haesler[25], T. Hasegawa[9], A. Herve[4], M. Hierholzer[24], J. Hylen[26], S. Igolkin[21], A. Ivashkin[18], S.R. Johnson[28], K. Kadija[2], A. Kapoyannis[7], E. Kaptur[14], J. Kisiel[14], T. Kobayashi[9], V.I. Kolesnikov[19], D. Kolev[1], V.P. Kondratiev[21], A. Korzenev[25], K. Kowalik[12], S. Kowalski[14], M. Koziel[6], A. Krasnoperov[19], M. Kuich[15], A. Kurepin[18], D. Larsen[13], A. László[8], M. Lewicki[16], B. Lundberg[26], V.V. Lyubushkin[19], M. Maćkowiak-Pawłowska[17], B. Maksiak[17], A.I. Malakhov[19], D. Manić[22], A. Marchionni[26], A. Marcinek[13,16], A.D. Marino[28], K. Marton[8], H.-J. Mathes[4], T. Matulewicz[15], V. Matveev[19], G.L. Melkumov[19], B. Messerly[29], G.B. Mills[27], S. Morozov[18,20], S. Mrówczyński[11], Y. Nagai[28], T. Nakadaira[9], M. Naskręt[16], M. Nirkko[24], K. Nishikawa[9], T. Palczewski[12], A.D. Panagiotou[7], V. Paolone[29], M. Pavin[3,2], O. Petukhov[18,20], C. Pistillo[24], R. Płaneta[13], B.A. Popov[19,3], M. Posiadała[15], S. Puławski[14], J. Puzović[22], R. Rameika[26], W. Rauch[5], M. Ravonel[25], A. Redij[24], R. Renfordt[6], E. Richter-Wąs[13], A. Robert[3], D. Röhrich[10], E. Rondio[12], M. Roth[4], A. Rubbia[23], B. Rumberger[28], A. Rustamov[0,6], M. Rybczynski[11], A. Sadovsky[18], K. Sakashita[9], K. Schmidt[14], T. Sekiguchi[9], I. Selyuzhenkov[20], A. Seryakov[21], P. Seyboth[11], D. Sgalaberna[23], M. Shibata[9], M. Słodkowski[17], P. Staszel[13], G. Stefanek[11], J. Stepaniak[12], H. Ströbele[6], T. Šuša[2], M. Szuba[4], M. Tada[9], A. Taranenko[20], D. Tefelski[17], V. Tereshchenko[19], R. Tsenov[1], L. Turko[16], R. Ulrich[4], M. Unger[4], M. Vassiliou[7], D. Veberič[4], V.V. Vechernin[21], G. Vesztergombi[8], L. Vinogradov[21], A. Wilczek[14], Z. Włodarczyk[11], A. Wojtaszek-Szwarc[11], O. Wyszyński[13], L. Zambelli[3,9], E.D. Zimmerman[28], and R. Zwaska[26]

[0] National Nuclear Research Center, Baku, Azerbaijan

[1] Faculty of Physics, University of Sofia, Sofia, Bulgaria

[2] Ruđer Bošković Institute, Zagreb, Croatia

[3] LPNHE, University of Paris VI and VII, Paris, France

[4] Karlsruhe Institute of Technology, Karlsruhe, Germany

[5] Fachhochschule Frankfurt, Frankfurt, Germany

[6] University of Frankfurt, Frankfurt, Germany

[7] University of Athens, Athens, Greece

[8] Wigner Research Centre for Physics of the Hungarian Academy of Sciences, Budapest, Hungary

[9] Institute for Particle and Nuclear Studies, Tsukuba, Japan

[10] University of Bergen, Bergen, Norway

[11] Jan Kochanowski University in Kielce, Poland

[12] National Centre for Nuclear Research, Warsaw, Poland
[13] Jagiellonian University, Cracow, Poland
[14] University of Silesia, Katowice, Poland
[15] University of Warsaw, Warsaw, Poland
[16] University of Wrocław, Wrocław, Poland
[17] Warsaw University of Technology, Warsaw, Poland
[18] Institute for Nuclear Research, Moscow, Russia
[19] Joint Institute for Nuclear Research, Dubna, Russia
[20] National Research Nuclear University, Moscow, Russia
[21] St. Petersburg State University, St. Petersburg, Russia
[22] University of Belgrade, Belgrade, Serbia
[23] ETH Zürich, Zürich, Switzerland
[24] University of Bern, Bern, Switzerland
[25] University of Geneva, Geneva, Switzerland
[26] Fermilab, Batavia, USA
[27] Los Alamos National Laboratory, Los Alamos, USA
[28] University of Colorado, Boulder, USA
[29] University of Pittsburgh, Pittsburgh, USA

1 Introduction

This NA61 annual report presents briefly the status and plans of the NA61/SHINE experiment [1] at the CERN SPS. The report refers to the period October 2014 – October 2015.

The document is organized as follows. An overview of the 2014 and 2015 data-taking period on p+Pb interactions at 158 GeV/c and Ar+Sc collisions at 13A GeV/c–150A GeV/c is given in Section 2. An overview on the detector maintenance and upgrades is given in Sec. 3. Progress in software and calibration as well as new results released in 2015 are briefly reviewed in Sections 4 and 5, respectively. Plans for data taking in 2016–2018 are outlined in Section 6. Finally, possible extensions of the approved physics programme are discussed in Section 7, namely a collision energy scan with Pb+Pb interactions to be performed in 2016 and 2018 is described and ideas of measurements beyond 2020 are sketched. The envisaged Pb+Pb interaction studies are presented in detail in a separate document submitted in parallel to this Status Report. The summary in Section 8 closes the paper.

2 Recorded data

In October NA61/SHINE completed data-taking on p+Pb interactions at 158 GeV/c. The first sample of p+Pb interactions at 158 GeV/c was registered in 2012. This run was stopped due to a failure of the VTX-2 magnet.

In February–April 2015, NA61/SHINE collected data on Ar+Sc collisions at 13A, 19A, 30A, 40A, 75A and 150A GeV/c. This data completed the energy scan with Ar+Sc collisions. This first NA61/SHINE data taking with primary ion beams was an important success.

The statistics on the recorded events are:

p+Pb	158 GeV/c	22.0 M events
Ar+Sc	13A GeV/c	3.9 M events
Ar+Sc	19A GeV/c	4.2 M events
Ar+Sc	30A GeV/c	5.1 M events
Ar+Sc	40A GeV/c	3.0 M events
Ar+Sc	75A GeV/c	3.0 M events
Ar+Sc[1]	75A GeV/c	2.3 M events
Ar+Sc	150A GeV/c	3.0 M events

The statistics collected during the Ar+Sc data taking period are presented in Fig. 1. The figure also shows a visualisation of an example event recorded during this period.

[1] Data collected with 40 GeV/c magnetic field configuration due to failure of the VERTEX-2 magnet.

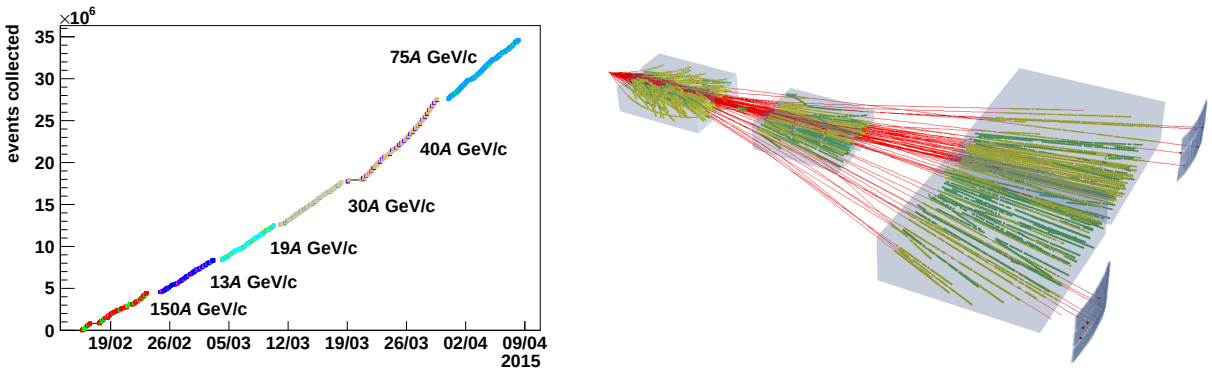

Figure 1: *Left:* Data on Ar+Sc central and semi-central collisions collected in NA61/SHINE as a function of time. *Right:* Example Ar+Sc collision at 150A GeV/c measured in the NA61/SHINE detector.

Due to the failure of the VERTEX-2 magnet, data taking of Ar+Sc at 75A GeV/c was divided into two periods: with the nominal magnetic field and a reduced magnetic field ("40A GeV/c" field). About 10% of the events were recorded with triggers needed for data quality control as well as corrections for off-target interactions and trigger bias.

The data taking for inelastic p+p interactions at 400 GeV/c planned in September 2015 as well as that planned for the Fermilab neutrino beams was cancelled due to the failure of the VTX-1 magnet, see Sec. 3.1 for details. The allocated beam time was used for detector tests and calibration runs.

3 Facility modifications

3.1 The upgrade and maintenance of the super-conducting magnets

During the past year the NA61/SHINE spectrometer magnets failed several times mostly due to failures of the cryogenic system.

The cryogenic and magnet system has been in operation for about 40 years. It includes critical, non-industrial components, especially to mention the liquid helium pumps, which have a short mean time between maintenance, high maintenance effort and a high failure rate between maintenance.

In 2015 considerable periods of the beam time were lost due to two major incidents.

On March 19, during the data taking with argon beam one of two helium pumps of the VERTEX-2 magnet failed. As a quick repair was not possible, representatives of PH, TE/CRG, EN, BE and NA61/SHINE agreed that by running the installation in its degraded state, the magnetic field could be set for data taking with 75A GeV/c beam momentum, corresponding to 13% of the maximum power dissipation. The magnet was then successfully operated until end of the run on April 7.

After warming up the system in April, no evident damage on the element in question was found, and it was assumed blocking with ice had been the origin of the problem. All helium pumps of both VERTEX-1 and VERTEX-2 underwent regular maintenance in June 2015.

Before the data taking period of September 2015, the system was flushed with warm helium gas in order to remove humidity and prevent the recurring of the problem described above. Three out of four diffusion pumps for cryogenic vacuum have been replaced. The forth diffusion pump was found to be in an acceptable condition and it was decided to schedule its replacement after the end of the data taking period of 2015.

For the exchange of the diffusion pumps, the magnets were warmed up by natural warming during 2 month and subsequent slow breaking of the insulation vacuum.

At the beginning of September the water cooling circuits for the cryogenic system was switched from drinking water to raw water. As then it turned out the pressure in raw water circuit is inadequate for magnets and NA61/SHINE TPC LV operating simultaneously, thus the coldboxes, were re-connected back to drinking water supply. The modifications on the cooling water circuits did not delay the cool-down of the magnets for the run starting on September 9.

On September 9 (the first day of the NA61/SHINE proton beam period) during a test ramp of the magnets a resistive transition (quench) occurred during the current ramp down for the VERTEX-1 magnet at about 3000 A. The resistive transition was caused by an instability of the flow control for the cooling of the current leads, resulting in a disruption of the helium flow in the current leads for about 10 minutes.

Following the investigation by PH-ADO, the VERTEX-1 magnet shows an excessive resistance between one current lead and the coil, making further operation impossible. This resistance is probably caused by the failure of the current lead cooling.

The severity of the damage and the possibility for a repair can only be assessed after a complete warm-up of the magnet.

For future operation, an improved magnet protection system is strongly recommended.

3.2 The Projectile Spectator Detector upgrade

The Projectile Spectator Detector (PSD) measures number of non-interacting nucleons (spectators) from a projectile nucleus in nucleus-nucleus collisions. The PSD is necessary both for the selection of event centrality at the trigger level and in the off-line analysis to minimise event-by-event fluctuations of the number of collision participants. After the upgrade of temperature stabilization and slow control systems in 2012-2014 the PSD operates in rather stable condition. During 2015 long-term Ar+Sc runs the stability of temperature of PSD photo-detectors was kept at about 0.01°C. The long term stability of micro-pixel avalanche photodiode (MAPD) signals was controlled with LED monitoring system with the accuracy of about $\pm 1\%$ which is sufficient for the control of the MAPD gains.

Muon calibration and tests of PSD with proton beams were performed in 2012-2014. Figure 2 presents the amplitude spectra for muons and the shape of the ADC pedestals (*left*). Wide pedestal peak is caused by the pick-up noises of the thermo-electrical controllers (TEC) used in the cooling system with the Peltier elements. Nevertheless, the muon ADC peaks are well separated from the pedestals and are used for the energy calibration of all PSD modules. The energy deposition spectra from the protons with different energies are shown in Fig. 2 (*right*). The obtained data confirmed the expected performance of the PSD and its ability to detect single nucleons.

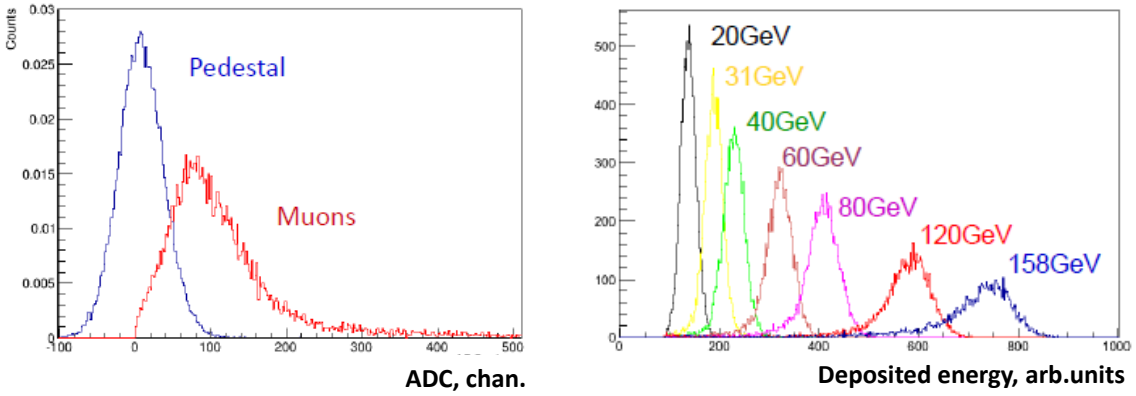

Figure 2: Amplitude spectra for muons (*left*) and protons with different energies (*right*).

During the 2015 Ar+Sc runs the PSD was placed at a distance of 17-22 m downstream from the target depending on the ion beam energy changing from 13A GeV to 150A GeV. In spite of reliable PSD operation in Ar+Sc runs a few potential problems for future runs with heavy ion beams were revealed. All these problems are associated with the peculiarity of hadronic showers and huge energy depositions in PSD for the heavy ions. For example, lead ion of 150A GeV beam would deposit in PSD energy of more than 30 TeV. At the same time, the PSD must be able to detect a single spectator with the energy starting from 13A GeV. As follows from these considerations, the PSD energy scale must have a wide dynamic range of about 2000 that would require a special tuning of the Front-End-Electronics (FEE) and readout.

The second problem with heavy ion detection is the long hadronic shower profile. It was found that in Ar+Sc collisions due to the long, hadronic shower, with respect to p+p interactions, about 12% of initial heavy ion energy escapes through the rear side of calorimeter.

The last problem is associated with the internal properties of photo-detectors, MAPDs, used for the light readout in the PSD. In spite of high pixel density and wide dynamic range, the recovery time of MAPD pixels is rather long. Since the PSD has no beam hole the central PSD module is irradiated with a high intensity ion beam and huge energy depositions. As a consequence, MAPDs in this module are illuminated by

frequent light pulses of high amplitudes that cause the pixel saturation and a decrease of the number of active pixels.

In order to improve the PSD performance in future heavy ion runs the following upgrades are planned. First, to improve the leak tightness for the hadronic showers of heavy beam ions an additional short module will be installed in front of the central PSD module. Second, the central modules of the PSD, as well as the new short module will be equipped with new fast MPPC photodetectors. Third, to increase the dynamic range of FEE in central modules the gains of amplifiers will be reduced. Below we consider these modifications in details.

3.2.1 Construction of short central module

As mentioned above, heavy beam ions have a large longitudinal hadronic shower profile. As a consequence, a significant part of hadronic shower (about 12%) escapes through the rear side of calorimeter that leads to the underestimated detected beam energy and affects the accuracy of the PSD trigger threshold. To fix this problem it was decided to install an additional short module in the PSD centre where the beam ions enter into hadron calorimeter. This small module consists of 12 lead/scintillator layers with 16 mm and 4 mm thickness, respectively. The lead/scintillator plates are tied together and placed in a box made of 0.5 mm thick steel. The transverse sizes of module equal to 10×10 cm^2. The full length of a module corresponds to 1.2 nuclear interaction lengths compared with 5.7 interaction lengths of the standard PSD modules.

Light read-out is provided by Kuraray Y11 wavelength shifting (WLS) fibres embedded in round grooves in the each scintillator plates. In the standard PSD modules the WLS-fibres from each 6 consecutive scintillator tiles are collected together in a single optical connector at the end of module, where the photo-detectors and the readout electronics are installed. The situation is quite different for the short central module. Since the radiation conditions for this module are much harder, it was decided to install the photodetectors and readout electronics separately in the readout module outside the beam region at the distance of about 1 meter from the beam axis. Therefore, the light from the scintillators is transported to the readout module trough long WLS-fibres that are glued into optical connectors in the readout module. In similar way, the WLS-fibres from each 6 consecutive scintillator tiles are collected together in a single optical connector in the readout module. Respectively, it has two optical connectors.

At present all the components for the short and readout modules are ready and are assembled at the NA61/SHINE area. The schematic drawing and photograph of the assembled short module are presented in Fig. 3.

3.2.2 New photo-detectors

The light of WLS-fibres in PSD calorimeter is read out by micropixel avalanche MAPD-3A photodiodes with the size 3×3 mm^2. These photodiodes have high dynamic range due to high density of about 10^4 pixels/mm^2 that is well matched for the calorimetrical

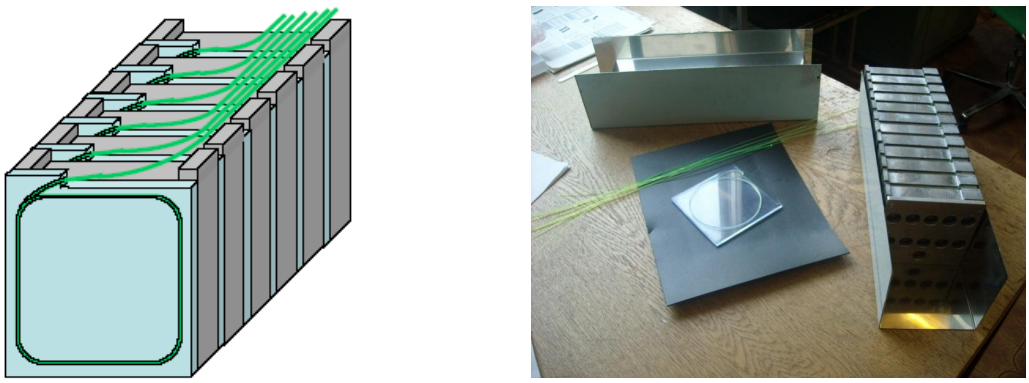

Figure 3: Schematic drawing and photograph of the assembled short module.

applications. At the same time, these photodiodes were developed in 2008 and the production technology that time was imperfect. Namely, the recovery time of the pixels reaches a few microseconds and might become significant at the count rates of 10^5 Hz. In this case some fraction of fired pixels is not recovered between the neighbour events that lead to the drop of the signal amplitude. This amplitude drop is observed in the central module when it is irradiated by a high intensity heavy ion beam. According to the measurements with argon beam the signal amplitude from these beam ions is reduced by about 9%. As a consequence, the beam energy deposition is underestimated that affects the accuracy of the PSD trigger threshold.

To avoid the above drawback it was decided to replace MAPD-3A photodiodes in central modules by fast silicon photomultipliers recently developed by Hamamatsu Co. Recently Hamamatsu Co. announced MPPC photodiodes with pixel density of 10000/mm^2. The pixel sizes are 10×10 μm^2 for MPPC's S12572-010C/P. The recovery time of the pixels as well as the length of the single electron pulses is less than 10 ns. During the light pulse from WLS-fibre (60 ns) each pixel can be recharged up to 4–6 times, and the equivalent pixel density could achieve up to 40000/mm^2 which is a very impressive number even for calorimetric applications. Note, that the photon detection efficiency of new photo-detectors is about 12% and rather similar to that for MAPD-3A photo-diodes, see Fig. 4. New MPPCs are mounted on the electronic boards instead of the previous MAPD-3A photo-diodes.

3.2.3 New Front-End-Electronics for central modules

The use of new photo-detectors in central PSD modules and the need of large dynamic range require the modification of the Front-End-Electronics (FEE). A photo of new electronic board with modified FEE is presented in Fig. 5. The photo-diodes of a single module are mounted on an aluminium plate that provides a common thermal contact to all 10 photo-diodes. The plate is cooled by a Peltier element and stabilized the MPPC

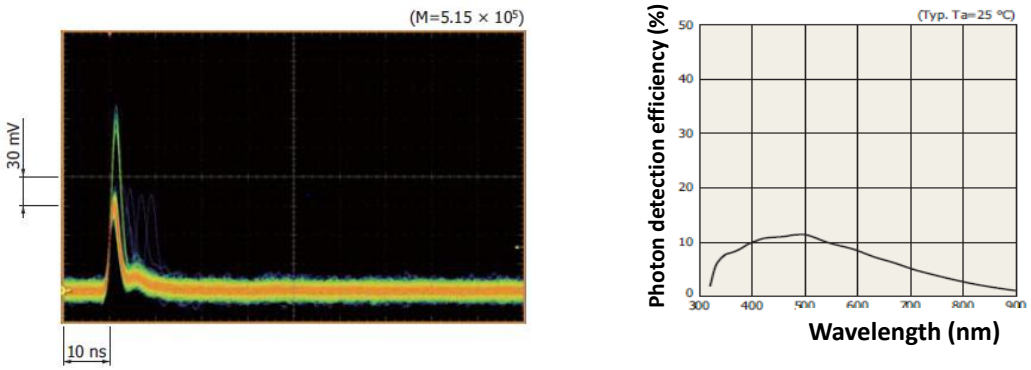

Figure 4: Single electron pulses of MPPC with the high pixel density (*left*) and photon detection efficiency (*right*).

temperature with the accuracy of about 0.01°C. Additionally, the photo-diodes are surrounded by the thermo-isolation to avoid the thermal contact with the surrounding air. The amplifiers for MPPC are placed at the opposite side of the electronic board, see Fig. 5 (*right*). To extend the dynamic range two amplifiers are used in each readout channel. First amplifier has a gain equal 4 and is used for the detection of high energy deposition from heavy ions. The second amplifier has an additional amplification factor of 10 and is used to detect muons during the energy calibration and also to detect single nucleons.

At present, two new electronic boards are prepared to be installed in the short and central modules. The performance of new readout channels will be examined during the Pb+Pb ion run in November 2015. After the tests it would be decided to produce a few pieces of the electronic boards for the PSD modules around the beam axis, where the count rate is maximum.

3.3 The extension of the drift velocity monitoring system

As Time Projection Chambers (TPC) are the main tracking detectors of the NA61/SHINE detector, measurement of electrons' drift velocity is of crucial importance. Current system has been inherited from the NA49 experiment. Although it was well designed and fully met NA49 needs, it was built in the mid-1990s and has become difficult to maintain, let alone to extend by additional chambers. Due to the use of obsolete technology and non-standard components, no spare parts are now available. Even the newest NA49 chamber, GAP TPC, has not been included in the system. NA61/SHINE also plans to introduce at least two new Forward TPCs. Thus, although the system is operational, it clearly needs an upgrade.

In the existing system, the drift velocity is measured in small drift chambers inserted in the gas system. The gas is ionized by α sources, and the signal is detected by wire detectors. The chambers require high voltage for the drift field, as well as for the

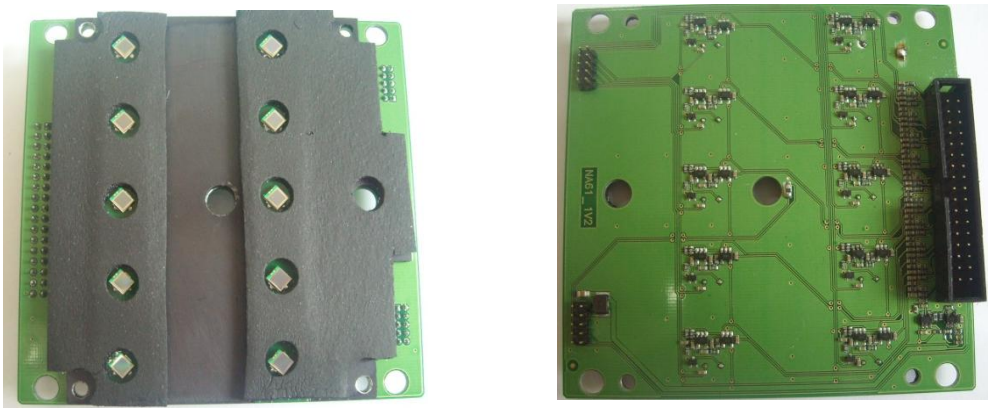

Figure 5: Photo of new photodetectors, MPPCs, mounted on the common board (*left*) and FEE (*right*).

readout wires. The signals are digitized by waveform analysers. Additionally, the gas temperature and pressure are measured in order to take into account the gas density variation. The measurement sequence is controlled and repeated automatically by the Detector Control System (DCS). The system upgrade plan includes construction of new measurement chambers with the detection structure identical to the existing one and development of a new readout and control system. The new readout for each TPC consists of PicoScope 3406B PC oscilloscope (200 MHz sampling rate), digital temperature sensor (Dallas 18B20) and pressure sensors BMP180 (BMP183 in the future) connected to a Raspberry Pi B computer communicating with the DCS via Ethernet. The system also includes programmable high-voltage power supply module for the drift voltage in the monitoring unit.

A prototype of an automatic drift velocity measurement in GAP TPC was provided and successfully tested during data taking. Also, new readout chain based on PicoScope digital oscilloscopes was installed and successfully tested. The accuracy of developed measurement system is of order of few per mill, what allows to reconstruct particle tracks with precision of order of millimetres. Prototype measurement chambers were successfully tested at the University of Warsaw. One of them was delivered to CERN for further tests in experimental conditions. New three chambers with full readout chain will be installed in NA61/SHINE in the spring 2016 to provide drift velocity monitoring in FTPCs. More readout channels could be easily added in the future if needed.

Moreover a portable pressure monitoring system (based on BMP180 sensors) is being developed in order to monitor conditions in existing drift velocity monitors as well as in FTPCs.

3.4 New beam detectors for primary ion beams

The heavy ion beams bring new challenges and require modifications of the beam detector setup. Beam interactions upstream of the target reduce data taking efficiency and may lead to systematic biases due to a beam contamination by nuclear fragments. One of the main solutions for this problem is to minimise the beam interaction before the target. This purpose can be achieved by decreasing the amount of material in the beam line.

One of the possible places where the amount of material can be decreased is to replace the scintillators detectors by thinner ones. Two new scintillator detectors were installed and used during the Argon data taking campaign. These detectors replaced the old S1 and S2 scintillators and have following properties:

- new S1 counter with $60 \times 60\,\mathrm{mm}^2$ BC-420 plastic scintillator [2] (thickness 0.5 mm) read by four photo-multipliers (PMT) ($2\times$ Photonis XP2020Q [3] and $2\times$ Hamamatsu R2059 [4]),
- new S2 counter with $40 \times 40\,\mathrm{mm}^2$ BC-420 plastic scintillator (thickness 0.5 mm) read by one Hamamatsu R2059 photo-multiplier.

This modification decreased the nuclear interaction length of material in the beam line by a factor of 2 from 1.355% to 0.592%.

Additional possible modification on the beam line to minimise the beam interaction before the target is to place all beam detectors into vacuum beam pipes. Since the existing beam position detectors (BPDs) cannot fulfil this requirement it is necessary to design new BPDs. Detectors based on fibre scintillators (Sci-Fi) employing 250 μm double cladding rounded scintillating fibres (SCSF-81M) from Kuraray are considered. For the test purposes the prototype of the detector which consist two planes of orthogonal fibres was constructed, see Fig. 6. The fibres are glued together and two layers of the fibres are used in each plane. Light is read from one side of the ribbon by silicon photomultiplier matrix (SiPMT). The prototype of the detector was tested in the H4 and H2 beam areas. As the test beam we used primary Argon beam and secondary proton beam at momenta of $13A$ GeV/c and 158 GeV/c respectively. We tested:

- Position resolution of the detector,
- Detector answer for different kind of ions i.e. Argon and proton,
- Read out electronics chain,
- DRS4 chip as main component of the read-out electronics,
- Cross talk between the fibres,
- Saturation of the SiPMT.

The data analysis of the test is in progress.

Figure 6: The prototype of the Sci-Fi detector.

3.5 The DRS-based read-out upgrade

The NA61/SHINE readout electronics has been inherited from the NA49 experiment. We decided to replace and upgrade the old electronics using the DRS digitizer developed at PSI [5]. The development of the new readout electronics is ongoing. For details on the overall structure and functioning of the new DRS readout see the 2013 and 2014 Status Reports.

A series of DRS readout prototype boards have been successfully developed and tested at the University of Geneva. The intrinsic time resolution is better than 10 ps. Further improvements are expected using a newly calibration/processing scheme under development. Among various advantages, this upgrade will add multi-hit capabilities to the ToF, which at present are missing, and timing information to various subdetectors, like the BPDs and the PSD. The design of the final electronics has been completed. Soon we will start the layout of the electronic boards. A first set of boards is expected for early 2016 and the system will be first tested on the forward ToF detector and PSD calorimeter. If successful, the mass production of the new electronics will start in spring 2016 and will be deployed toward the end of summer 2016.

Table 1 summarizes the number of DRS channels required for the upgrade of the NA61/SHINE readout. It also shows the various sampling frequencies at which the DRS will be operated and the corresponding acquisition windows (buffer depths) for each sub-system. Around 500 DRS4 chips, including spares, are required to upgrade the NA61/SHINE readout.

sub-system	# of ch.	# DRS chips	# DRS boards	sampling f. (MHz)	buffer depth (ns)
ToF-R	891	112	28	5000	200
ToF-L	891	112	28	5000	200
ToF-F	160	20	5	5000	200
PSD	440	55	14	800	1250
PSD deep buffer	32	32	4	800	10000
beam (trigger)	64	8	2	5000	200
beam deep buffer	8	8	1	800	10000
BPD	384	48	12	800	1250
BPD deep buffer	24	24	3	800	10000

Table 1: Number of DRS readout channels required for each sub-system, including the sampling frequencies and acquisition windows for each sub-system. Each DRS boards comprises 4 DRS4 chips and has 32 channels.

3.6 The extension of the TPC tracking system: Forward TPCs

The forward tracking subproject is intended to allow the measurement of secondary protons in the moderate- to high-x region. This is primarily motivated by interaction studies for the neutrino program, where these protons are responsible for up to 25% of the ν_μ flux in the NuMI beam and likely a comparable fraction in the LBNF beam. A secondary goal of the system is to measure the high-momentum part of the π^+ production.

The NA61/SHINE detector is designed primarily to track particles that bend out of the beam; only one small tracking detector, the GAP TPC (GTPC), covers the forward region. We are instrumenting the forward region with two TPCs, one immediately upstream and one immediately downstream of the MTPCs. The new TPCs will have electric field and readout geometry based largely on the existing NA61/SHINE TPCs, and will use existing spare electronics. One chamber will be placed immediately upstream of the MTPCs and the other (with two field cages) immediately downstream of the MTPCs (see Fig. 7).

3.6.1 Physics requirements and geometrical constraints

The new TPCs must cover the gap between the MTPC fiducial areas with several centimeters of overlap for cross-calibration. They must also be constructed with minimal material that could shadow the MTPCs. Ideally, the chambers should have enough extent in the longitudinal direction to separate protons from π^+ at momenta below $\sim$ 75 GeV/c. The upstream chamber will also sit in a relatively confined space approximately 78 cm wide in the longitudinal direction, with obstructing cable trays about 10 cm above the elevation of the MTPC field cage.

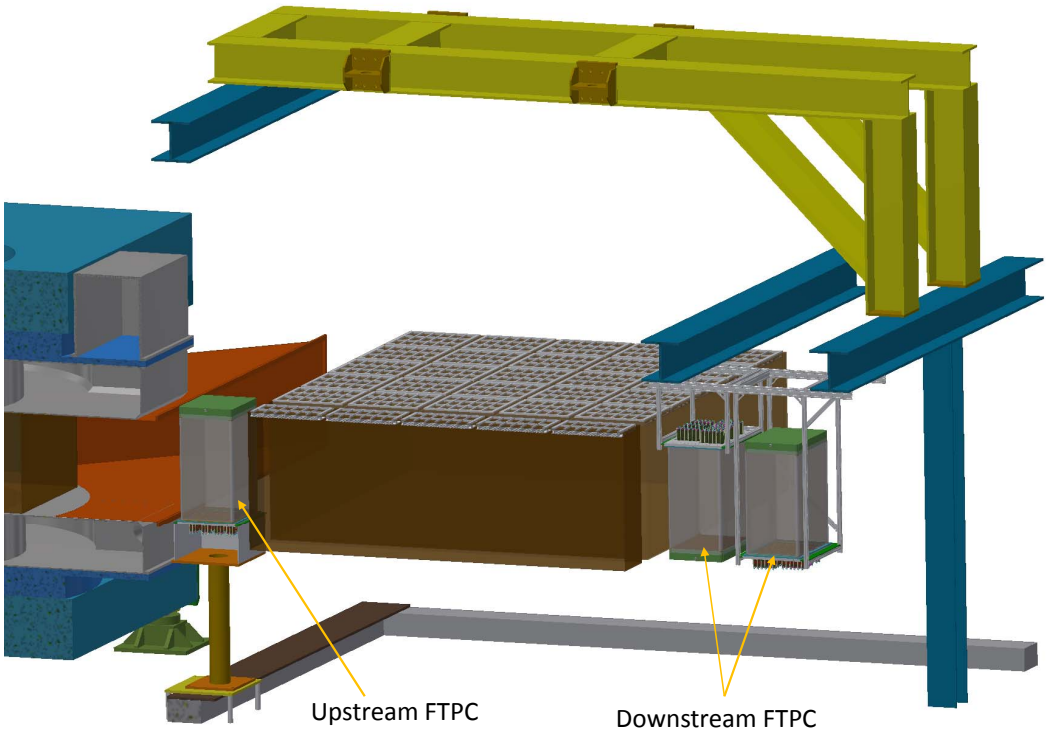

Figure 7: Cutaway view of the NA61/SHINE MTPC hut showing renderings of new forward TPCs. Image by Jan Boissevain

A final consideration is that, for heavy-ion physics, the chambers should be capable of reconstructing many-particle events. This, along with the availability of existing electronics, was the motivation for using TPCs instead of a series of drift chambers.

Higher-rate running conditions are expected to generate enough tracks in the beam region so that out-of-time tracks may produce significant backgrounds. Out-of-time tracks are reconstructed as spatially separated tracks. In order to reject these tracks, successive field cages will have opposite drift directions so out-of-time tracks will appear unconnected at chamber boundaries. This "tandem TPC" concept originated with the Budapest group and will be implemented for the first time here.

3.6.2 Design and construction plan

The chambers are being designed, to the extent practical, to take advantage of the existing infrastructure of NA61/SHINE. There are approximately 200 spare front-end boards, each of which serves 32 individual readout pads. A single motherboard serves 24 front-end boards; therefore the most efficient arrangement of channels is a multiple of 768. We plan to use two motherboards for the upstream chamber and four for the downstream chamber. This puts us within the limits of the existing spare electronics supply (and we have contingency plans in the case that multiple cards are nonfunctional). The

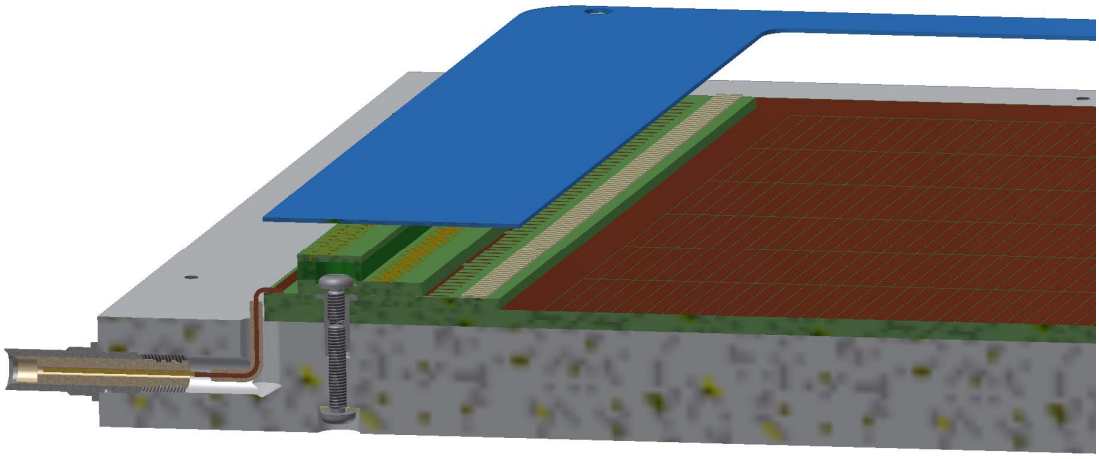

Figure 8: Readout pad plane and attachment boards for wire grids for the FTPCs. Image by Jan Boissevain.

drift high voltage supplies used by the other chambers are still in production and are being ordered from the same company.

The planned pad plane and wire grid geometry is shown in Fig. 8. The arrangement for the upstream chamber is the same as a single module of the MTPCs, with twelve full rows of 4×40 mm^2 pads. The downstream chamber will be a two-cage tandem system. The upstream and downstream pads will be of the normal size, with larger pads in the center in order to maximize dE/dx coverage while minimizing the channel count.

We will use an improvement to the field cage design of the existing chambers, which use a series of individually-clamped aluminized mylar strips that were difficult to assemble. The field cage and cathode will be made into a single detachable assembly (the "top hat," Fig. 9). The field cages will be made of etched polyamide films with divider resistors soldered directly to the film.

The chambers' gas system (which will use a simple one-way flow of Ar+CO_2, the same mixture used by the other TPCs in NA61/SHINE) will be built of standard parts and assembled in place at CERN. The collaboration will provide drift velocity monitors for the new chambers.

3.6.3 Assembly and installation plans

The design and most parts procurement are being handled by the University of Colorado, with input and collaboration from the Wigner Institute (KFKI) in Budapest. The initial pad plane assembly will be done in Colorado this autumn, then sent to Budapest where wire winding will be done at KFKI. The field cage and drift cathode materials will be procured in the US. The top hats will be assembled in a hall in the North Area, and then joined to the wire frames. Installation will occur in mid-summer 2016.

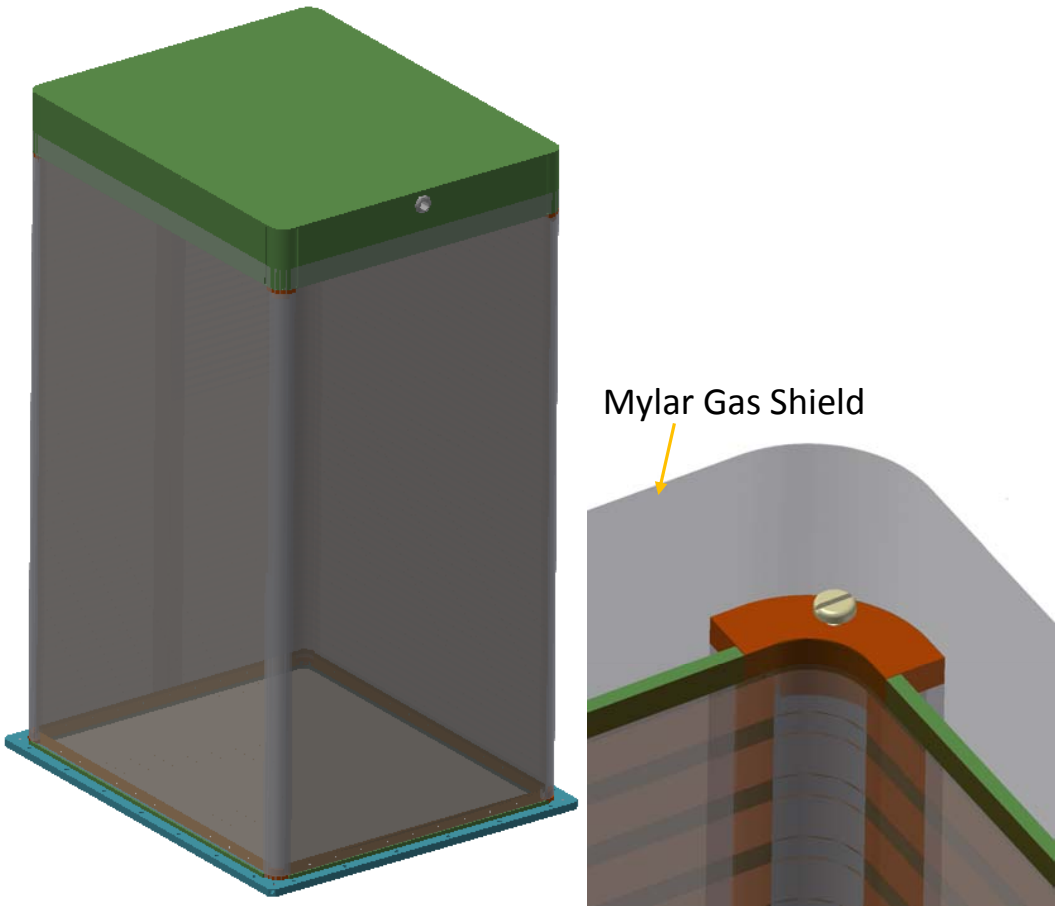

Figure 9: Left: "Top hat" consisting of field cage, gas buffer, and drift cathode assembly. Right: detail of field cage film and corner post. Image by Jan Boissevain.

4 Software and calibration modifications

4.1 The "legacy" software maintenance

Over the last year, we continued to maintain the "legacy" software. It is compiled on a dedicated 32-bit SLC5 Virtual Machine (VM) provided by CERN via the Cloud Infrastructure (https://openstack.cern.ch). The produced executables run under the SLC6 operating system. Only two "legacy" software releases have been made since the time of the last Status Report, introducing required bug-fixes and updates. Thanks to the progress with the new SHINE software framework, it was decided to minimise the "legacy" software support under SLC6 and to freeze its development.

Up to now, the "legacy" software is still routinely used within the collaboration to process raw data and to perform MC simulations.

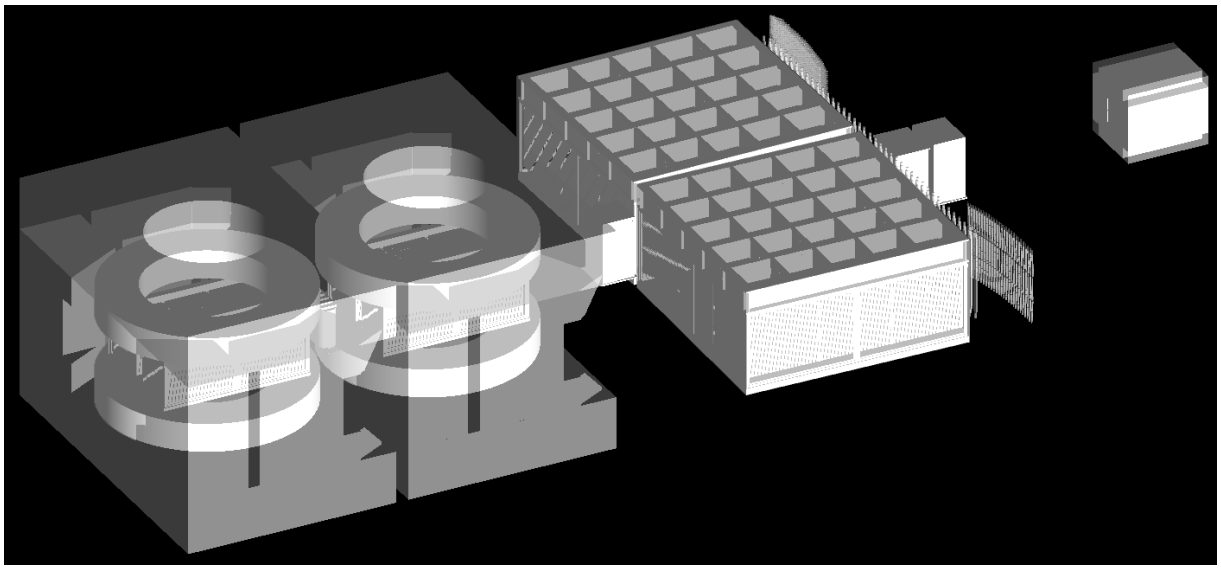

Figure 10: GEANT4 detector description in SHINE software. This is based on an the actual detector geometry used for 2009 p+C 31 GeV/*c* run with the addition of the F-TPCs located just upstream and downstream of the MTPCs.

4.2 The NA61/SHINE offline software development

4.2.1 MC simulation status and development

The "legacy" MC simulation relies on the GEANT3 simulation for the NA61/SHINE detector description. However, GEANT3 is becoming outdated and migration to the GEANT4 is highly recommended. Also, it is necessary to launch the "SHINE-native" MC simulation including new sub-systems (e.g. Vertex Detector, F-TPCs), since the "legacy" MC is not fully compatible with the new systems because of its software design concept.

A GEANT4 based detector description is fully implemented in the SHINE software, including the new sub-systems. Figure 10 shows an example of the GEANT4 detector description. After the particle transport through the detector is simulated with GEANT4, hits are recorded for the subsequent MC simulation steps. Optimization of the GEANT4 particle production threshold is under investigation.

GEANT4 hits are then fed into the digitization process which simulates the detector response and outputs raw detector simulated signals. The "legacy" FORTRAN code calculating the drift of charge clouds in the TPCs has been re-written in C++ to improve maintainability. An example of digitized data responses on TPC pads is shown in Fig. 11. For comparison, GEANT4 hits in the TPCs are also shown in Fig. 11. For other systems individual digitization algorithms are needed and they are under development.

The digitized MC data are fed either into the wrapped SHINE reconstruction chain or the SHINE-native reconstruction that is under development.

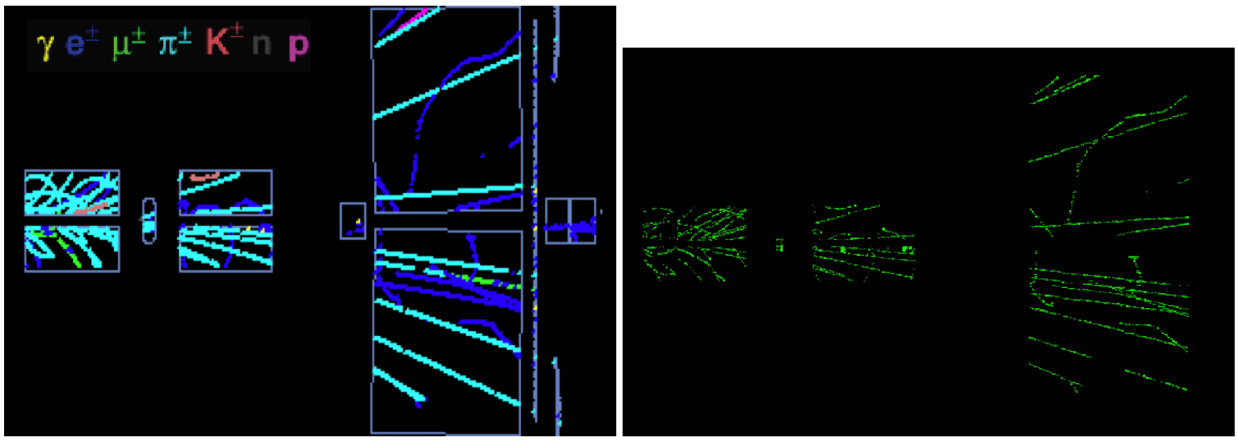

Figure 11: (*Left:*) GEANT4 simulated particles pass through detectors from left to right. (*Right:*) Response of digitized data on TPC pad planes for the same event shown in the left figure. The ADC values for each pad are not yet optimized.

4.3 The deployment of the Shine reconstruction

NA61/SHINE entered into the final phase of the implementation of the new software in the production chain. All of the necessary steps were already reached. The new SHINE software was validated over the "legacy" production chain and is ready for deployment. The last necessary ingredient which should be validated over the "legacy" reconstruction chain is the Monte-Carlo simulation. The process of validation is in progress and will be finished in the near future. Simultaneously the database information has started to be transferred to the new structures required by the SHINE production chain. Because the SHINE software still inherits some functions, modules and structures from the "legacy" reconstruction, the development of new modules is ongoing. An example is the development of a new track pattern recognition algorithm based on Bayes' theorem.

4.4 The calibration upgrade

An important implementation of the new software is the conversion of the present "legacy" calibration chain to the SHINE framework. In addition to allowing calibration to be performed using the modern software tools that are used in reconstruction, it will also allow the collaboration to restructure the full calibration process to be more efficient and streamlined. Some of the detector parameters needed for reconstruction are not known *a priori* but must be extracted during the calibration process using raw data. The most important and complex detector in NA61/SHINE is the TPC and therefore it garners the bulk of the calibration effort. In 2013 a software expert was hired by NA61/SHINE to convert the "legacy" software chain to SHINE. He developed a modular (i.e. "staged") program:

- Stage 1: MultiHitTDC (MHTDC) for beam time structure monitoring and TPC clock phase measurement calibration,
- Stage 2: Time-dependent drift velocity (v_{D}),
- Stage 3: Start time for TPC chambers (t_0),
- Stage 4: Vertical offset of the TPC chambers (y_0).

Stage 1 runs two modules. The first calibrates the time phase between the main timing counter (S1) and the TPC. The second module determines the calibration constants for the CAEN V1290N MHTDC. The MHTDC is used to determine the relative timing between the Main Trigger signal and the S1 with a timing resolution of 200 ps. Stage 2 calibrates the drift velocity of the TPC. Stage 3 determines t_0, the time offset of the delay of the drift time sampling with respect to the reference time determined from S1. Finally Stage 4 determines the vertical geometric offset of the TPC using the results of Stage 2 (v_{D}) and 3 (y_0). Presently all stages work under the S$\underline{\text{HINE}}$ framework but have only been tested on small data samples. Large sample tests are presently being performed.

The other main detector of NA61/SHINE is the ToF system. Presently the calibration of the ToF systems (Left, Right and Front) still uses the "legacy" software. Therefore the present effort in the calibration group is the conversion of the ToF calibration software to S$\underline{\text{HINE}}$. The ToF data are now usable in the SH⊛E format and therefore the present work involves migrating legacy ToF-L/R calibration software to the S$\underline{\text{HINE}}$ framework. Finally the magnetic field map has been ported to S$\underline{\text{HINE}}$ however discrepancies between the two field maps have been observed in certain regions of phase space that need to be resolved.

In summary much progress has been made in the conversion of the "legacy" calibration software to the S$\underline{\text{HINE}}$ framework over the last year but presently it is not complete. It is expected that the conversion, including large sample testing, should be finished over the next year.

4.5 NA61/SHINE IT infrastructure

The NA61/SHINE collaboration uses the CERN IT infrastructure as the main place to store, manage and analyse the data. The CERN CASTOR system serves as the main storage of the data. The collaboration uses also the EOS service to store data for physics analysis where the fast and easy access is required. Presently NA61/SHINE has allocated 200 TB (100 available for data storage) of space on the EOS service. The production and analysis processes use the CERN computing service (lxBatch). The recent increase in our share of resources (from 600 to 1200 kSi2K) allowed an increase in the efficiency of data production and analysis. The CERN cloud infrastructure (CERN OpenStack) is used by NA61/SHINE as the main place where services are moved. For now the electronic logbook, bookkeeping, and the application for software integrity checks (Jenkins) have already moved to the virtual environment. Development of a new quality assessment system under virtual technology is ongoing.

5 New results

5.1 New results for strong interaction physics

5.1.1 New results from Ar+Sc interactions

Spectra of π^- mesons in central ^{40}Ar+^{45}Sc collisions at 40A GeV/c and 150A GeV/c
The first spectra of negatively charged pions produced in Ar+Sc collisions were obtained using the so-called "h$^-$ method" [6]. The method is based on the fact, that the majority of negatively charged hadrons produced in high energy collisions are pions. The remaining small contamination ($\approx$ 10%) of other hadrons (K$^-$ and $\overline{\text{p}}$) is subtracted using Monte-Carlo models (EPOS1.99 [7]). Corrections for the geometrical acceptance, inefficiency of the reconstruction, losses due to cuts as well as feed-down from weak decays and secondary interactions are calculated using the detector simulation based on GEANT3 and the EPOS1.99 event generator. The Monte-Carlo generated central Be+Be collisions at corresponding beam momenta were used to obtain correction factors for this study.

The double differential spectra of transverse momentum p_T vs. cms rapidity y are shown in Fig. 12 for the 0–5% most central collisions, which were selected using the forward energy measured by the 28 inner modules of the Projectile Spectator Detector. This energy is referred as to forward energy and denoted E_F.

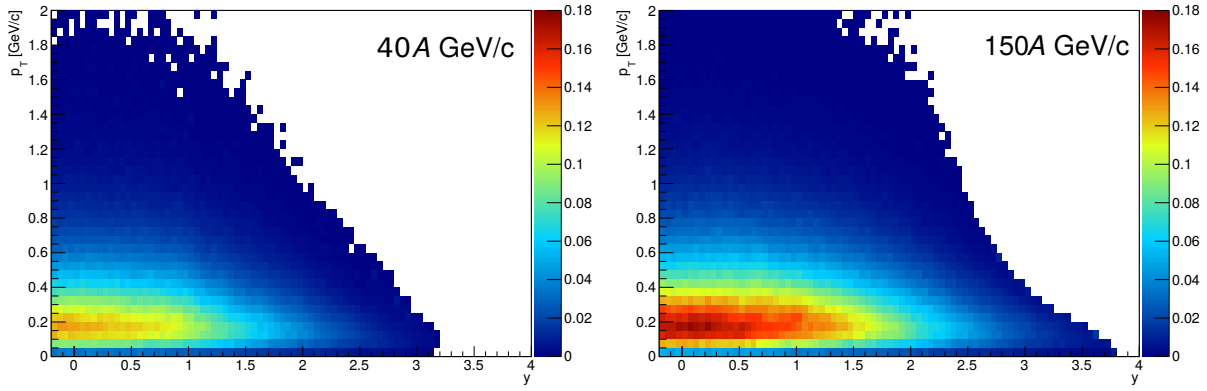

Figure 12: Double differential spectra $\left(\text{d}^2n/(\text{d}p_\text{T}\,\text{d}y)\right)$ of negatively charged pions in rapidity and transverse momentum for central Ar+Sc collisions at 40A (*left*) and 150A GeV/c (*right*).

The corresponding rapidity $(\text{d}n/\text{d}y)$ spectra together with the NA61/SHINE data on inelastic p+p interactions [6] and Be+Be most central collisions [8] are presented in Fig. 13.

Mid-rapidity transverse mass (m_T) spectra in central Ar+Sc collisions as well as the corresponding NA61/SHINE data on inelastic p+p interactions [6], central Be+Be colli-

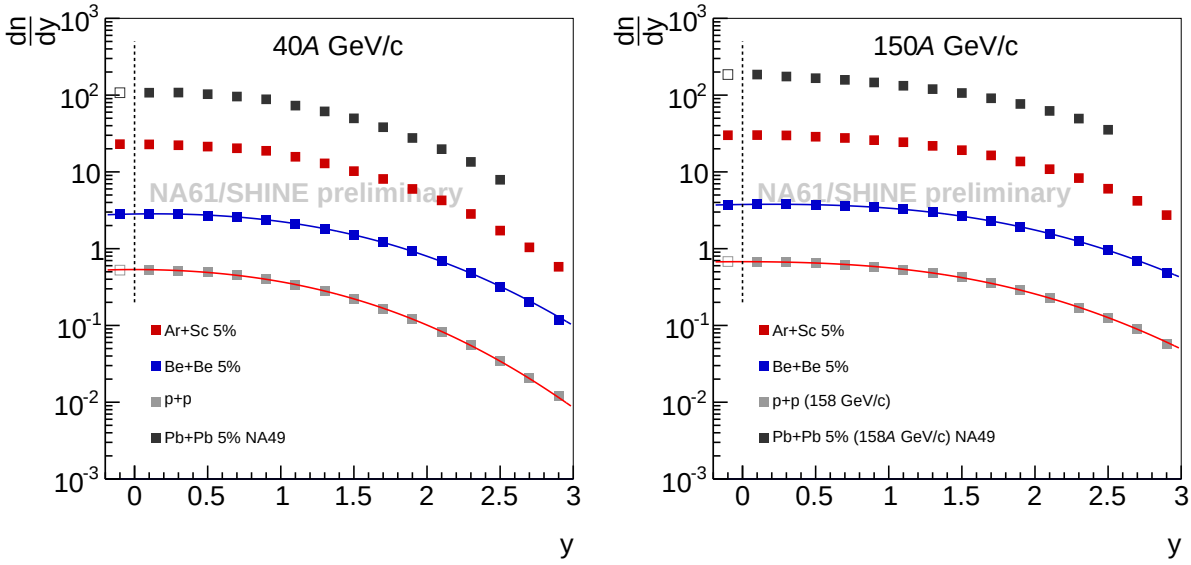

Figure 13: Rapidity spectra of negatively charged pions in central Ar+Sc collisions at 40A (*left*) and 150A GeV/c (*right*). Spectra for Be+Be most central collisions [8], inelastic p+p interactions [6] and the NA49 results on central Pb+Pb collisions [9] are shown for comparison.

sions [8] and the NA49 results on central Pb+Pb collisions [9] are presented in Fig. 14. Transverse mass spectra were fitted in the range $0.2 < m_{\mathrm{T}} - m_{\pi} < 0.7$ GeV/c^2 with the exponential function:

$$\frac{\mathrm{d}^2 n}{\mathrm{d}y\,\mathrm{d}m_{\mathrm{T}}} = A \cdot m_{\mathrm{T}} \cdot \exp\left(-\frac{m_{\mathrm{T}}}{T}\right) . \tag{1}$$

In hydrodynamic models the shape of transverse mass spectra reflects the transverse velocity of the collective flow and the temperature of the matter at freeze-out. With more hadrons being produced, i.e. with increasing system size and collision energy, the hydrodynamical phase is expected to last longer. This in turn should lead to an increase of the collective velocity and the corresponding modification of transverse mass spectra. The spectra presented in Fig. 14 deviate more and more from the fit with increasing size of colliding nuclei. This may be caused by the collective flow increasing with the system size.

Multiplicity fluctuations in central Ar+Sc collisions at 150A GeV/c Multiplicity distributions of negatively charged hadrons produced in central Ar+Sc collisions at 150A GeV/c were obtained as the first step of the fluctuation study in this reaction. In order to minimize the fluctuations in the number of wounded nucleons, the analysis used only the 1% most central collisions selected with the forward energy measured in the PSD. The results were obtained in two acceptances: the NA61/SHINE acceptance and the NA49 broad (NA49-B: no VTPC-1 only tracks; pion rapidity range $0 < y_{\pi} < y_{\mathrm{beam}}$)

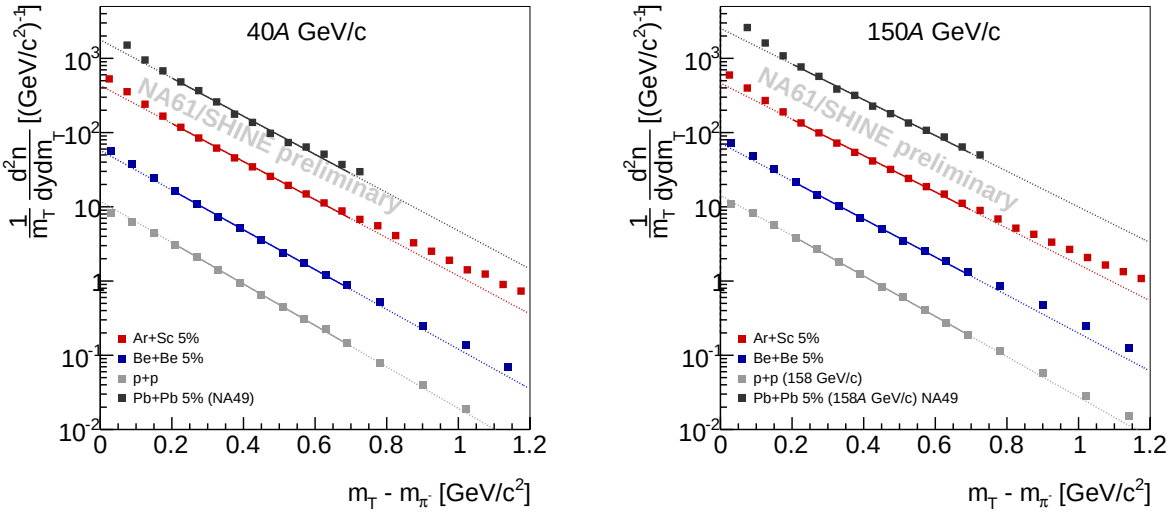

Figure 14: Transverse mass spectra of negatively charged pions at mid-rapidity in central Ar+Sc collisions at 40A GeV/c and 150A GeV/c. The corresponding spectra for inelastic p+p interactions (NA61/SHINE) [6], central Be+be collisions [8] and central Pb+Pb collisions (NA49) [9] are shown for comparison.

acceptance. The latter was compared with the corresponding results from NA49 on C+C, Si+Si and Pb+Pb collisions [10–12].

The analysis was performed for negatively charged hadrons as the resulting distributions and fluctuations are weakly influenced by decays of resonances [13]. The multiplicity distribution of negatively charged hadrons is shown in Fig. 15 (*top*) in linear (*left*) and logarithmic (*middle*) scales. For comparison a Poisson distribution with the same mean multiplicity is plotted. Figure 15 (*right*) presents the ratio between data and Poisson distributions, here only points with statistical uncertainties smaller than 20% are shown. In Fig. 15 (*bottom*) the corresponding distributions are presented for the NA49-*B* acceptance. The multiplicity distributions in the NA49-*B* and in the NA61/SHINE acceptances are both narrower than of the Poisson. This implies that the scaled variance of multiplicity distribution:

$$\omega[N] = \frac{\mathrm{Var}(N)}{\langle N \rangle} = \frac{\langle N^2 \rangle - \langle N \rangle^2}{\langle N \rangle} \tag{2}$$

is smaller than one (the value for the Poisson distribution).

In order to make a direct comparison of the scaled variances with ones calculated in p+p collisions and with NA49, data corrections for detector effects, trigger bias and non-target interactions are needed. Based on the analysis of inelastic p+p interactions [14] these corrections are estimated to be small. Therefore multiplicity fluctuations in the 1% most central Ar+Sc collisions are suppressed in comparison to inelastic p+p interactions, where the scaled variance is significantly larger than one [14].

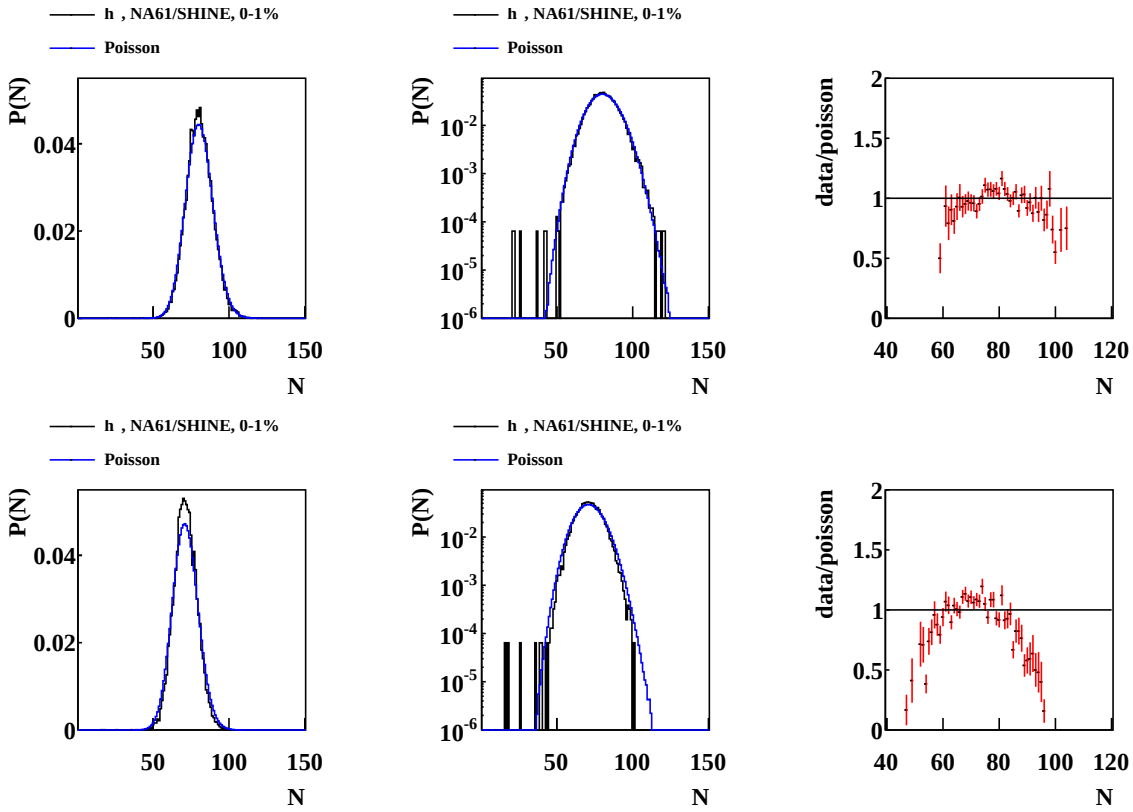

Figure 15: Multiplicity distribution of negatively charged hadrons in the 1% of most central Ar+Sc collisions at 150A GeV/c within acceptance of NA61/SHINE (*top*) and NA49 (*bottom*). Comparison with the Poisson distribution in linear (*left*) and logarithmic (*middle*) scales. Black lines indicate data, and blue lines show a Poisson distribution with the same mean multiplicity as in data. *Right*: The ratio of the measured multiplicity distribution to the corresponding Poisson one.

In the following discussion, this difference is compared with the the Wounded Nucleon Model (WNM) [15] and the Statistical Model (SM) [16] of particle production. These models are selected because they are simple and play a special role in analysing the physics of heavy ion collisions.

The Wounded Nucleon Model [15] assumes that particle production in nucleon-nucleon and nucleus-nucleus collisions is an incoherent superposition of particle production from wounded nucleons (nucleons which interacted inelastically and whose number is calculated using the Glauber approach). Properties of wounded nucleons are assumed to be independent of the size of the colliding nuclei, e.g. they are the same in p+p and Ar+Sc collisions for a given collision energy per nucleon. The scaled variance of the multiplicity distribution of produced particles calculated within the WNM reads [17]:

$$\omega[N] = \omega^*[N] + \langle N \rangle / \langle W \rangle \cdot \omega[W] \,, \tag{3}$$

where W is the number of wounded nucleons and $\omega^*[N]$ denotes the scaled variance calculated for any fixed value of W. The number of wounded nucleons (protons) in p+p interactions is fixed at two, and the measured scaled variance for p+p interactions can be used as $\omega^*[N]$. The second term on the right-hand side of Eq. (3) vanishes or is positive. Consequently the WNM predicts that the scaled variance in nucleus-nucleus collisions has to be equal to or larger than the one in inelastic proton-proton interactions. The NA61/SHINE results presented in Fig. 15 (*top*) clearly contradict this prediction.

The Statistical Model of multi-particle production was proposed by Fermi in 1950 [16]. Its basic assumption states that all possible micro-states of the macroscopic system created in a collision are equally probable. For a non-interacting (ideal) gas of Boltzmann particles in the grand canonical ensemble (IB-GCE) the multiplicity distribution is Poissonian ($\omega[N] = 1$) and independent of the (fixed) system volume. Resonance decays and Bose effects increase the scaled variance from 1 to 1.1, whereas the conservation laws reduce it if the system volume is sufficiently large [13]. In fact the results for the 1% most central Ar+Sc collisions are well described by the hadron gas model in the micro-canonical ensemble (HG-MCE) [13]. Within the statistical models a scaled variance significantly larger than one as measured in inelastic p+p interactions at high collision energies (top SPS and higher) can be understood as a result of volume and/or energy fluctuations [18].

5.1.2 New results from Be+Be and p+p interactions

π^- spectra in Be+Be collisions Preliminary double differential spectra (in cms rapidity y and transverse momentum p_T) of negatively charged pions produced in Be+Be collisions at 20A and 30A GeV/c were obtained using the so-called "h^- method" [6].

Corrections for the geometrical acceptance, inefficiency of the reconstruction, losses due to cuts as well as feed-down from weak decays and secondary interactions are calculated using the detector simulation based on GEANT3 and the EPOS1.99 event generator.

The spectra were obtained in four centrality classes: 0–5%, 5–10%, 10–15%, and 15–20%. The centrality is determined as a fraction of total inelastic cross-section obtained from the measured PSD energy spectrum.

The pion spectra in Be+Be collisions were previously presented in the 2013 and 2014 Status Reports. The results presented here (see Fig. 16) refer to the lower beam momentum data taken in 2013. The low beam momentum data is characterized by worse beam quality (much wider and divergent) than beam at higher momenta. The results are presented, like results from the 2014 Status Report, in an extended rapidity acceptance. The acceptance in transverse momentum p_T extends up to 1.5 GeV/c.

Rapidity spectra of negatively charged pions were obtained from the double differential spectra in y and p_T (Fig. 16) by integrating over available transverse momentum acceptance and extrapolating a small contribution ($< 1\%$) in the high p_T region with an exponential function.

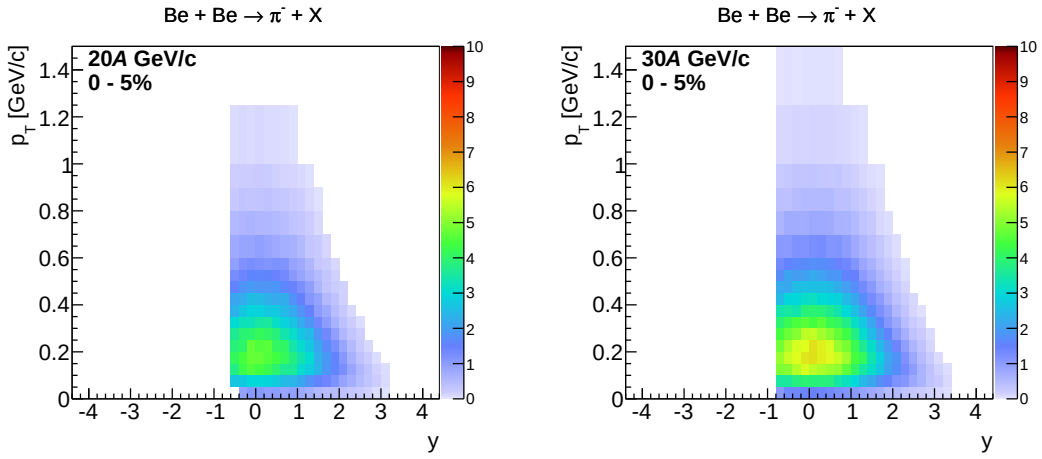

Figure 16: Double differential spectra of negatively charged pions in rapidity and transverse momentum for Be+Be interactions at 20A and 30A GeV/c.

The spectra were fitted with two Gaussian functions symmetrically displaced from mid-rapidity. The fitted Gaussian functions have the same widths but, due to asymmetry of the colliding system (^{7}Be+^{9}Be) and event selection, different amplitudes. The extension of the acceptance to the backward rapidity made it possible to perform a stable fit.

Example rapidity spectra for 20A and 150A GeV/c beam momenta are shown together with data from p+p interactions in Fig. 17.

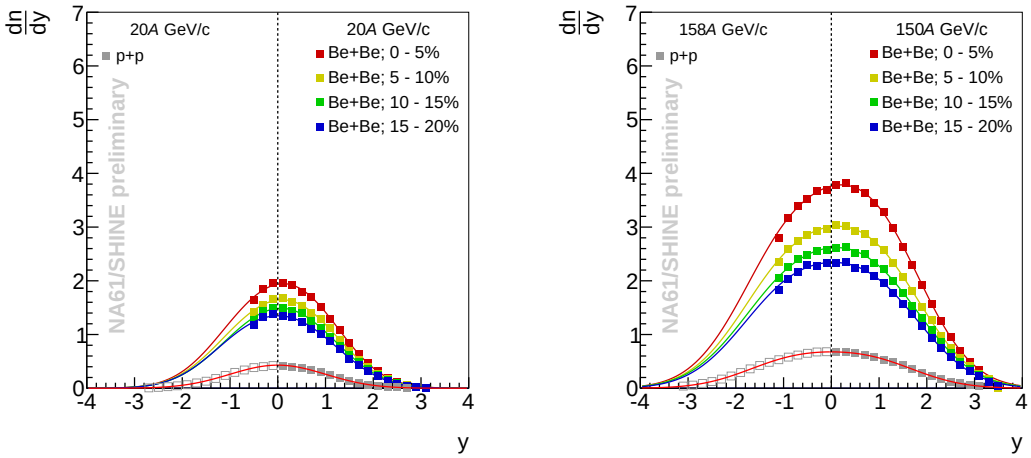

Figure 17: Rapidity spectra of π^- mesons produced in ^{7}Be+^{9}Be and inelastic p+p interactions at 20A GeV/c *(left)* and 150A GeV/c *(right)*.

The width of the spectra was calculated as a standard deviation of the fitted function. The widths of the rapidity distribution divided by the beam rapidity for the five beam

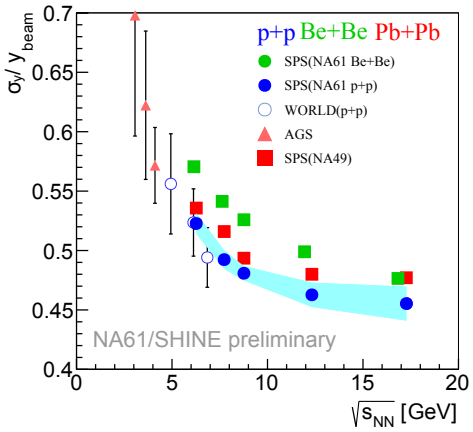

Figure 18: Width of the rapidity distribution of π^- mesons divided by the beam rapidity as a function of collision energy for p+p, ^{7}Be+^{9}Be and Pb+Pb interactions.

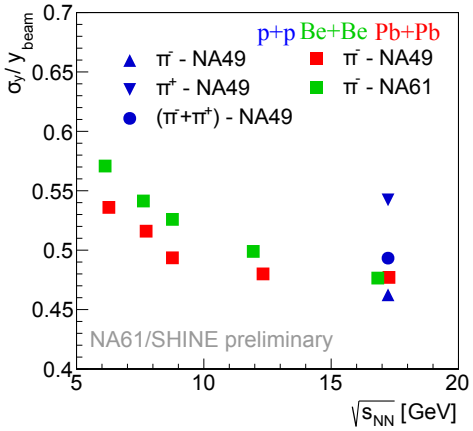

Figure 19: Width of the rapidity distribution of π^- mesons produced ^{7}Be+^{9}Be (*green*) and Pb+Pb (*red*) interactions divided by the beam rapidity as a function of collision energy. At 158 GeV/c the width for the π^-, π^+ and $\pi^+ + \pi^-$ mesons in p+p (*blue*) interactions is shown [20].

momenta for the most central ^{7}Be+^{9}Be collisions are shown together with the world data for p+p and Pb+Pb interactions [9,19] in Fig. 18.

The width of the rapidity distribution of negatively charged pions is monotonic with collision energy. However, at any given beam energy, the dependence of the width on the system size is non-monotonic. The width of the p+p distribution is the smallest one, Pb+Pb is in the middle, while ^{7}Be+^{9}Be is the largest.

In comparison with ^{7}Be+^{9}Be and Pb+Pb collisions, p+p interactions have a large isospin asymmetry. The simplest way to account for the isospin effects is to calculate the average spectra of negatively and positively charged pions. The only available data on positively charged pion spectra in a large acceptance in inelastic p+p interactions at 158 GeV/c are from NA49 experiment [20]. At this beam momentum the difference in the width of the rapidity distribution for different system sizes is the smallest. Nevertheless, by taking into account the isospin asymmetry of p+p interactions the monotonicity of the width of the rapidity distribution as a function of system size is restored (see Fig. 19).

The transverse mass spectra at mid-rapidity for four centrality classes of ^{7}Be+^{9}Be collisions as well as inelastic p+p and central Pb+Pb collisions are shown in Fig. 20. The spectra were fitted with an exponential function in the range $0.2 \leq m_{\mathrm{T}} - m_{\pi} \leq 0.7$ GeV/c^2.

The p+p data are well fitted by the exponential function, while both ^{7}Be+^{9}Be and Pb+Pb data deviate from the exponential fit at both low and high m_{T}.

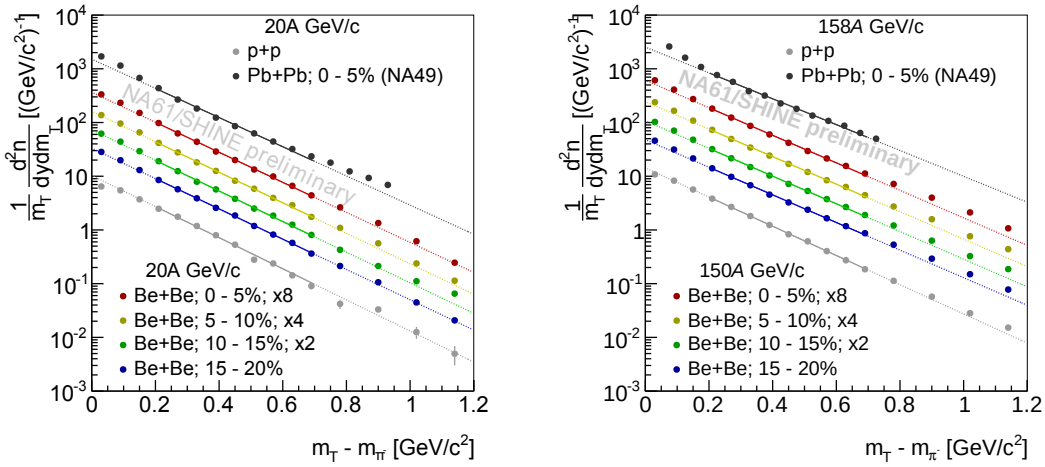

Figure 20: Transverse mass spectra of π^{-} mesons for ^{7}Be+^{9}Be, p+p and Pb+Pb interactions at 20A GeV/c (*left*) and 150A GeV/c (*right*).

In order to compare shapes of transverse mass spectra of negatively charged pions for various system sizes the ratio of normalized transverse mass spectra for ^{7}Be+^{9}Be/p+p and Pb+Pb/p+p was calculated (see Fig. 21). Both ratios, ^{7}Be+^{9}Be/p+p and Pb+Pb/p+p, have the same structure. In the high m_{T} region the ratio increases. This increase, and the corresponding decrease at intermediate transverse masses, are usually attributed to the collective flow. The effect is less pronounced in ^{7}Be+^{9}Be/p+p ratio. Furthermore, in the Pb+Pb data no beam momentum dependence is visible, while in the Be+Be data, the increase of the ratio at the high m_{T} seems to be larger for higher beam momenta, which is visible in Fig. 22. Such an effect might suggest dependence of the magnitude of collective effects on the increasing beam momentum in ^{7}Be+^{9}Be collisions.

The detailed explanation of the observed structures requires further analysis.

Transverse momentum and multiplicity fluctuations in Be+Be collisions Figure 23 shows the scaled variance of multiplicity distribution ($\omega[N]$) for Be+Be and p+p interactions. The results from p+p collisions [21] are fully corrected for contributions from non-target interactions and for other biases (losses due to event and track selections and reconstruction inefficiency and background of non-primary charged hadrons). The methods of correcting results were discussed in previous reports. Results on Be+Be collisions are corrected for non-target interactions and the correction for trigger bias and other detector effects is expected to be small. The centrality for Be+Be collisions was determined from the energy deposited in PSD.

$\omega[N]$ increases with energy – probably due to KNO scaling [22] (variance of the multiplicity distribution increases faster than its mean). Larger values for Be+Be than for

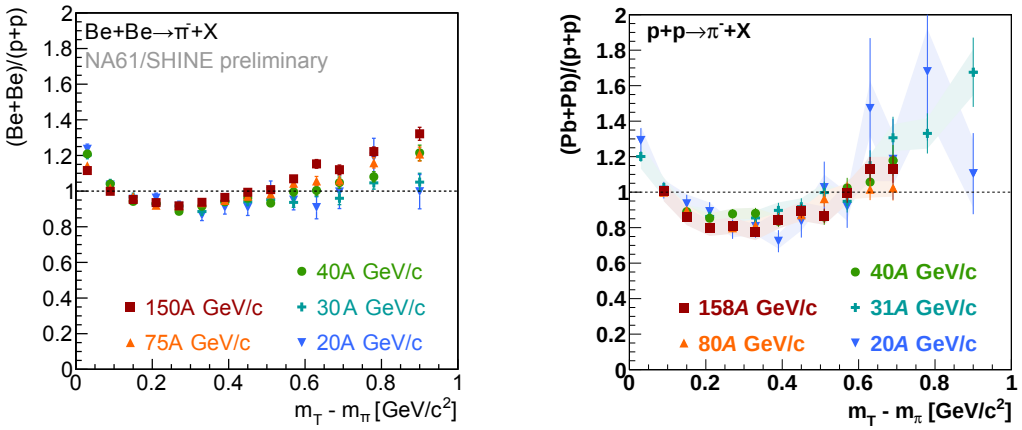

Figure 21: Ratio of normalized transverse mass spectra for different system sizes. *Left*: ^{7}Be+^{9}Be/p+p; *Right*: Pb+Pb/p+p.

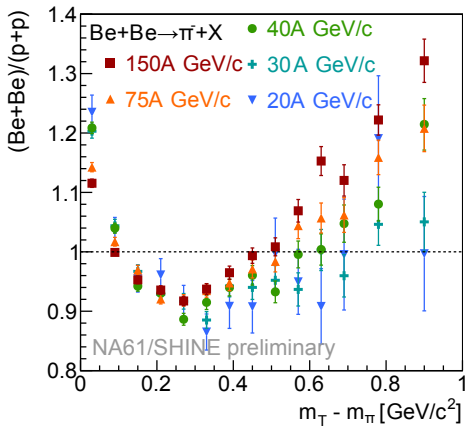

Figure 22: Ratio of normalized transverse mass spectra for ^{7}Be+^{9}Be/p+p. Note the ratio at $(m_T - m_\pi) > 0.6\,\mathrm{GeV}/c^2$ increasing with increasing collision energy suggesting increase of collective effects with beam momentum.

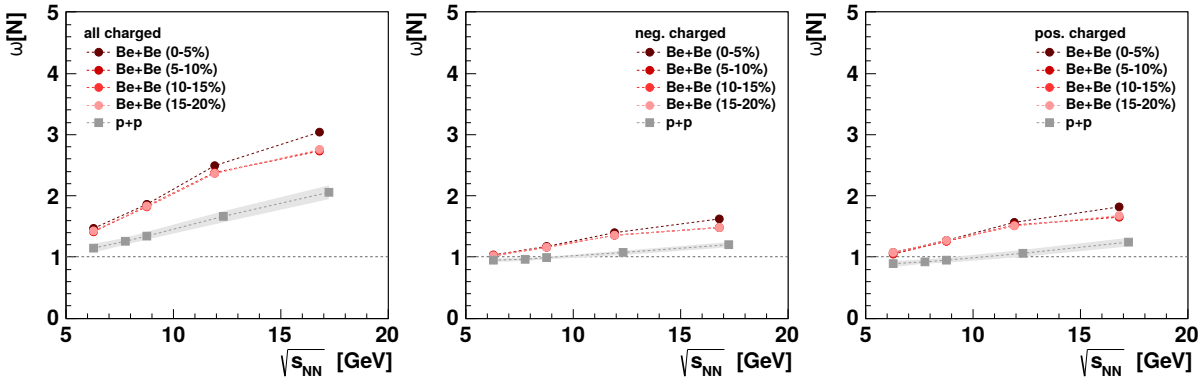

Figure 23: $\omega[N]$ measure of multiplicity fluctuations in p+p and Be+Be collisions in NA61/SHINE.

p+p collisions are probably due to volume fluctuations because $\omega[N]$ is not a strongly intensive measure. In order to compare the scaled variances for Be+Be collisions with

results for C+C, Si+Si, Pb+Pb collisions from the NA49 Collaboration [10–12] more restrictive centrality selection is needed.

The preliminary NA61/SHINE results on transverse momentum and multiplicity fluctuations, expressed in terms of Δ and Σ measures, are presented in Figs. 24 and 25. Based on the event observables particle multiplicity N and sum of moduli of their transverse momenta $P_{\mathrm{T}} = \sum_{i=1}^{N} |p_{\mathrm{T}}|_i$ one defines:

$$\Delta[P_{\mathrm{T}}, N] = \frac{1}{\langle N \rangle \omega(p_{\mathrm{T}})} [\langle N \rangle \omega[P_{\mathrm{T}}] - \langle P_{\mathrm{T}} \rangle \omega[N]] \tag{4}$$

and

$$\Sigma[P_{\mathrm{T}}, N] = \frac{1}{\langle N \rangle \omega(p_{\mathrm{T}})} [\langle N \rangle \omega[P_{\mathrm{T}}] + \langle P_{\mathrm{T}} \rangle \omega[N] - 2(\langle P_{\mathrm{T}} N \rangle - \langle P_{\mathrm{T}} \rangle \langle N \rangle)] \,, \tag{5}$$

where

$$\omega[P_{\mathrm{T}}] = \frac{\langle P_{\mathrm{T}}^2 \rangle - \langle P_{\mathrm{T}} \rangle^2}{\langle P_{\mathrm{T}} \rangle} \,, \tag{6}$$

and

$$\omega[N] = \frac{\langle N^2 \rangle - \langle N \rangle^2}{\langle N \rangle} \,. \tag{7}$$

The quantity $\omega(p_{\mathrm{T}})$ is the scaled variance of the inclusive p_{T} distribution (summation runs over all particles and all events).

The values of $\Delta[P_{\mathrm{T}}, N]$ and $\Sigma[P_{\mathrm{T}}, N]$ are equal to zero in the absence of event-by-event fluctuations (N = const., P_{T} = const.) and equal to one for fluctuations given by the independent particle production model (IPM).

Transverse momentum fluctuations in Be+Be and p+p interactions show no structures which could be related to the critical point. The Be+Be results are close to those from inelastic p+p reactions. The weak dependence on centrality in Be+Be shows that fluctuations do not depend on the collision volume. The difference between $\Delta[P_{\mathrm{T}}, N]$ and $\Sigma[P_{\mathrm{T}}, N]$ might be due to Bose-Einstein [23] and/or $P_{\mathrm{T}}/N - N$ anti-correlation [24].

The graphical presentation of the current status of search for the critical point in NA61/SHINE is presented in Fig. 25.

Charge fluctuations in Be+Be collisions at 150A GeV/c The new strongly intensive measures Δ and Σ have been recently used by NA61/SHINE to study charge fluctuations in Be+Be collisions at 150A GeV/c. For charge fluctuations, Δ and Σ are expressed as:

$$\Delta[N_+, N_-] = \frac{1}{\langle N_- \rangle - \langle N_+ \rangle} [\langle N_- \rangle \omega[N_+] - \langle N_+ \rangle \omega[N_-]] \,, \tag{8}$$

$$\Sigma[N_+, N_-] = \frac{1}{\langle N_- \rangle + \langle N_+ \rangle} [\langle N_- \rangle \omega[N_+] + \langle N_+ \rangle \omega[N_-] - 2(\langle N_+ N_- \rangle - \langle N_+ \rangle \langle N_- \rangle)] \,, \tag{9}$$

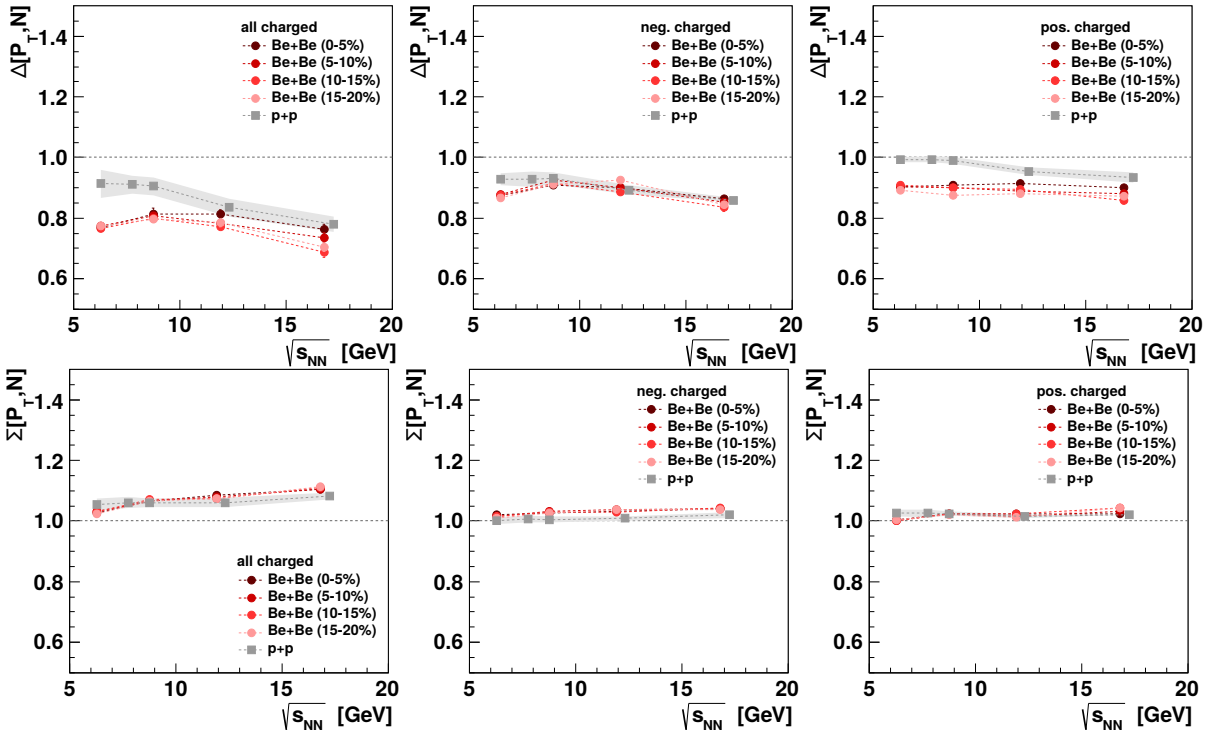

Figure 24: $\Delta[P_{\mathrm{T}}, N]$ and $\Sigma[P_{\mathrm{T}}, N]$ measures of transverse momentum and multiplicity fluctuations in p+p and Be+Be collisions in NA61/SHINE.

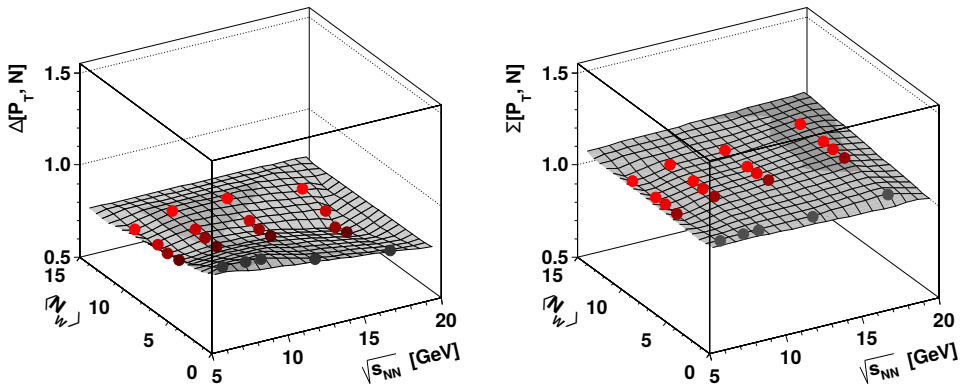

Figure 25: $\Delta[P_{\mathrm{T}}, N]$ and $\Sigma[P_{\mathrm{T}}, N]$ measures of transverse momentum and multiplicity fluctuations in p+p and Be+Be collisions in NA61/SHINE.

where N_+ and N_- are the multiplicities of positively and negatively charged hadrons within analysed kinematic acceptance, respectively, and ω is defined similarly as in Eq. (7). The denominators in Eqs. (8) and (9) were chosen in a way such that $\Delta[N_+, N_-]$ and $\Sigma[N_+, N_-]$ are equal to unity in the limit of the independent particle production model. Note that $\Sigma[N_+, N_-]$ is closely connected to the widely used quantity, $\nu_{(+-,\mathrm{dyn})}$ [25], that is used to measure net-charge fluctuations and is expected to be sensitive to the QGP formation.

The method of correcting the results is similar to the $[P_T, N]$ fluctuations analysis, but here instead of the subtraction of target-removed events, only events with the fitted interaction point placed very close to the center of target were selected. Corrections for detector effects and trigger bias were similar to $[P_T, N]$ fluctuations too (they were based on generated and reconstructed Monte Carlo events from EPOS1.99 [7]). Statistical uncertainties of fluctuation measures were calculated via the subsample method.

The analysis was performed for several $\delta\eta$ bins as shown in Fig. 26, thus the results could be sensitive to electric charge conservation and resonance decays. Moreover, it may allow the estimation of contribution coming from hadronic diffusion that happens between chemical and kinetic freeze-out [26].

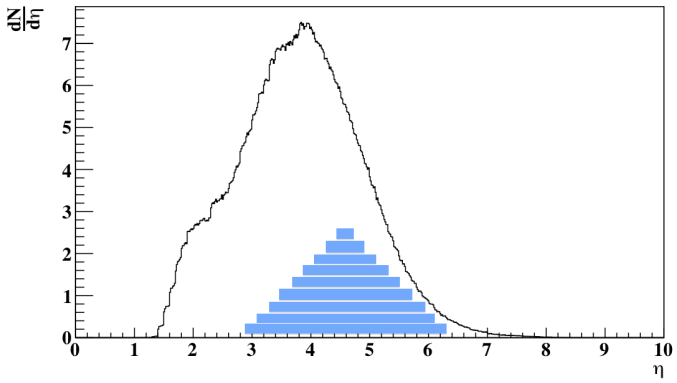

Figure 26: Nine pseudorapidity intervals used in the analysis of $\Delta[N_+, N_-]$ and $\Sigma[N_+, N_-]$. $\delta\eta = 0.2 + i \cdot 0.4$, $i = 0, \ldots, 8$.

The influence of corrections on charge fluctuations in Be+Be at 150A GeV/c is presented in Fig. 27. The corrections are of the order of several per cent.

The preliminary NA61/SHINE results on charged fluctuations in Be+Be at 150A GeV/c are shown in Fig. 28 and compared to EPOS1.99 model in Fig. 29. The $\Delta[N_+, N_-]$ and $\Sigma[N_+, N_-]$ measures are almost independent of centrality (although $\Delta[N_+, N_-]$ shows some deviations for larger $\delta\eta$) and both of them are smaller than one (this can be due to energy-momentum conservation and charge conservation effects). The value of $\Sigma[N_+, N_-]$ decreases significantly with growing $\delta\eta$. The behaviour of $\Delta[N_+, N_-]$ and $\Sigma[N_+, N_-]$ is well reproduced by the EPOS1.99 model; for $\Sigma[N_+, N_-]$ we see almost perfect agreement.

Pseudo-rapidity correlations in Be+Be at 150A GeV/c Pseudo-rapidity correlations are defined as correlations between observables B and F in different pseudo-rapidity windows. The correlation parameter is computed as:

$$b_{\mathrm{rel}}[B, F] = \frac{\langle F \rangle}{\langle B \rangle} \cdot \frac{\langle BF \rangle - \langle B \rangle \langle F \rangle}{\langle F^2 \rangle - \langle F \rangle^2}\,, \tag{10}$$

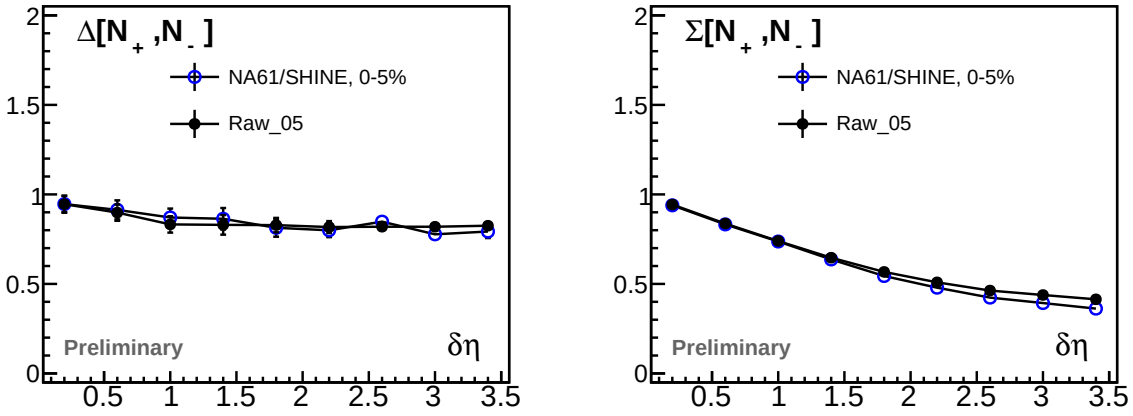

Figure 27: Example corrected (open blue circles) and uncorrected (full black circles) results on $\Delta[N_+, N_-]$ (*left*) and $\Sigma[N_+, N_-]$ (*right*) for 5% most central Be+Be collisions at 150A GeV/c.

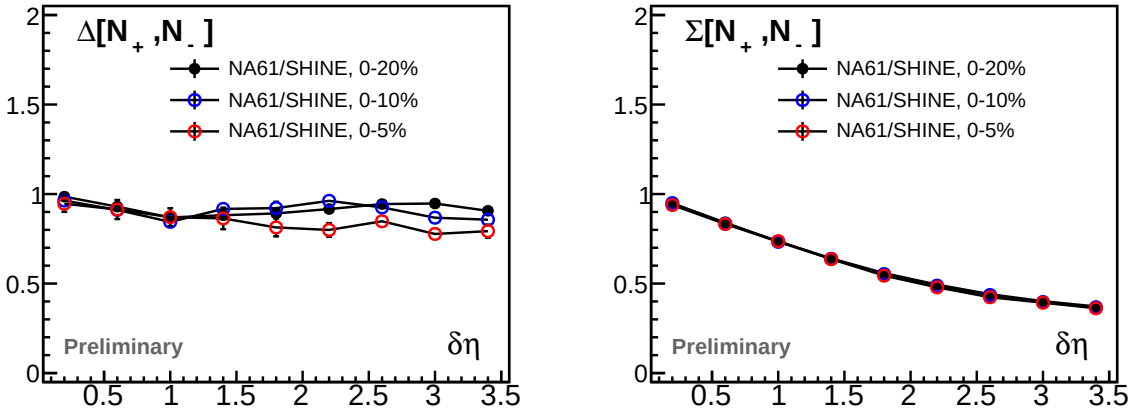

Figure 28: $\Delta[N_+, N_-]$ (*left*) and $\Sigma[N_+, N_-]$ (*right*) measures for different centrality classes of Be+Be collisions at 150A GeV/c. Statistical uncertainties are shown; systematic uncertainties are estimated to be lower than 5% for all points.

where $\langle B \rangle$ and $\langle F \rangle$ are the event averages of given observables in the "backward" and "forward" pseudo-rapidity windows, respectively. In this work we present the following types of pseudo-rapidity correlations:

1. Backward multiplicity N_{B} and forward multiplicity N_{F}: $b_{\mathrm{rel}}[N_{\mathrm{B}}, N_{\mathrm{F}}]$,
2. Backward mean transverse momentum Pt_{B} and N_{F}: $b_{\mathrm{rel}}[Pt_{\mathrm{B}}, N_{\mathrm{F}}]$,
3. Backward and forward mean transverse momenta Pt_{B} and Pt_{F}: $b_{\mathrm{rel}}[Pt_{\mathrm{B}}, Pt_{\mathrm{F}}]$.

The results were corrected for biases due to trigger, off-line selection, track and event selection, and other effects related to detection and reconstruction by using events ob-

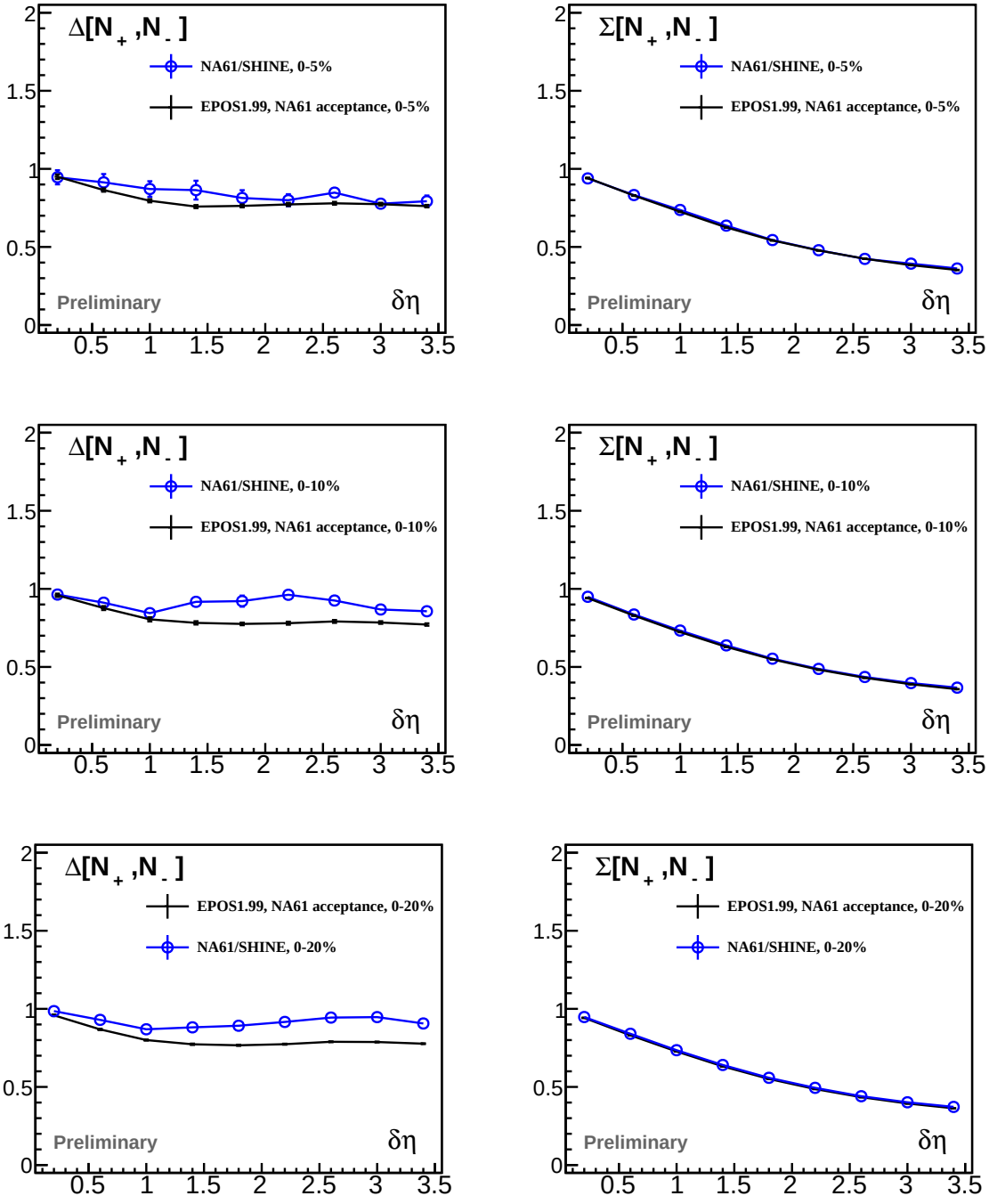

Figure 29: Comparison of the $\Delta[N_+, N_-]$ (*left*) and $\Sigma[N_+, N_-]$ (*right*) measures between NA61/SHINE (open blue circles) and EPOS1.99 model (black line). Three different centrality classes of Be+Be collisions are shown. Statistical uncertainties are shown; systematic uncertainties are estimated to be lower than 5% for all points.

tained from EPOS1.99 event generator with GEANT3 detector simulation and reconstruction. Electrons and positrons were removed with a dE/dx cut. Effects from hard scattering were reduced by a cut on particle transverse momentum $p_{\mathrm{T}} < 1.5$ GeV/c. All results were calculated inside NA61/SHINE acceptance. Only statistical errors are shown for pseudo-rapidity correlations.

We used two sets of η windows for the study of pseudo-rapidity correlations in Be+Be collisions at 150A GeV/c: short-range and with fixed forward window, see Fig. 30. A strong dependence of the correlations on the window position is observed. EPOS1.99 describes the data only qualitatively.

Figure 31 present the results for the short-range and separated windows, respectively. Correlations in pseudo-rapidity of multiplicity and mean transverse momentum strongly depend on the position of the chosen pseudo-rapidity windows. Significant multiplicity-mean transverse momentum long-range correlations were observed that might be a signal of collective effects.

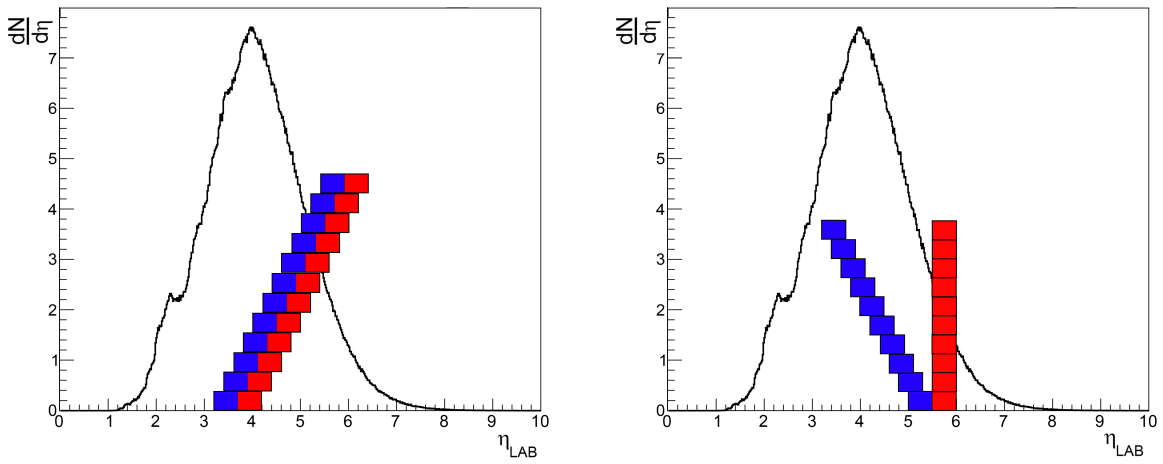

Figure 30: Illustration of connected (*left*) and disconnected (*right*) η windows. "Backward" windows are of blue color, "forward" - of red.

Mean multiplicities identified hadrons in inelastic p+p interactions The 4π multiplicities of negatively and positively charged π, K and p were calculated based on double differential spectra obtained with *tof*-dE/dx and dE/dx analysis methods. The spectra are extrapolated and interpolated in the non-measured p_{T} and y regions. First, the spectra are reflected with respect to mid-rapidity ($y = 0$). The reflection can be done thanks to the symmetry of the collision system. Second, the spectra are extrapolated to the non-measured low-p_{T} regions by the exponential function fit. Next, the distributions are extrapolated to high-p_{T} and integrated over p_{T}. Resulting integrated rapidity spectra are presented in Fig. 32. Statistical uncertainties, shown as a bars, are calculated as the square root of the summed squared statistical errors of measured point and the

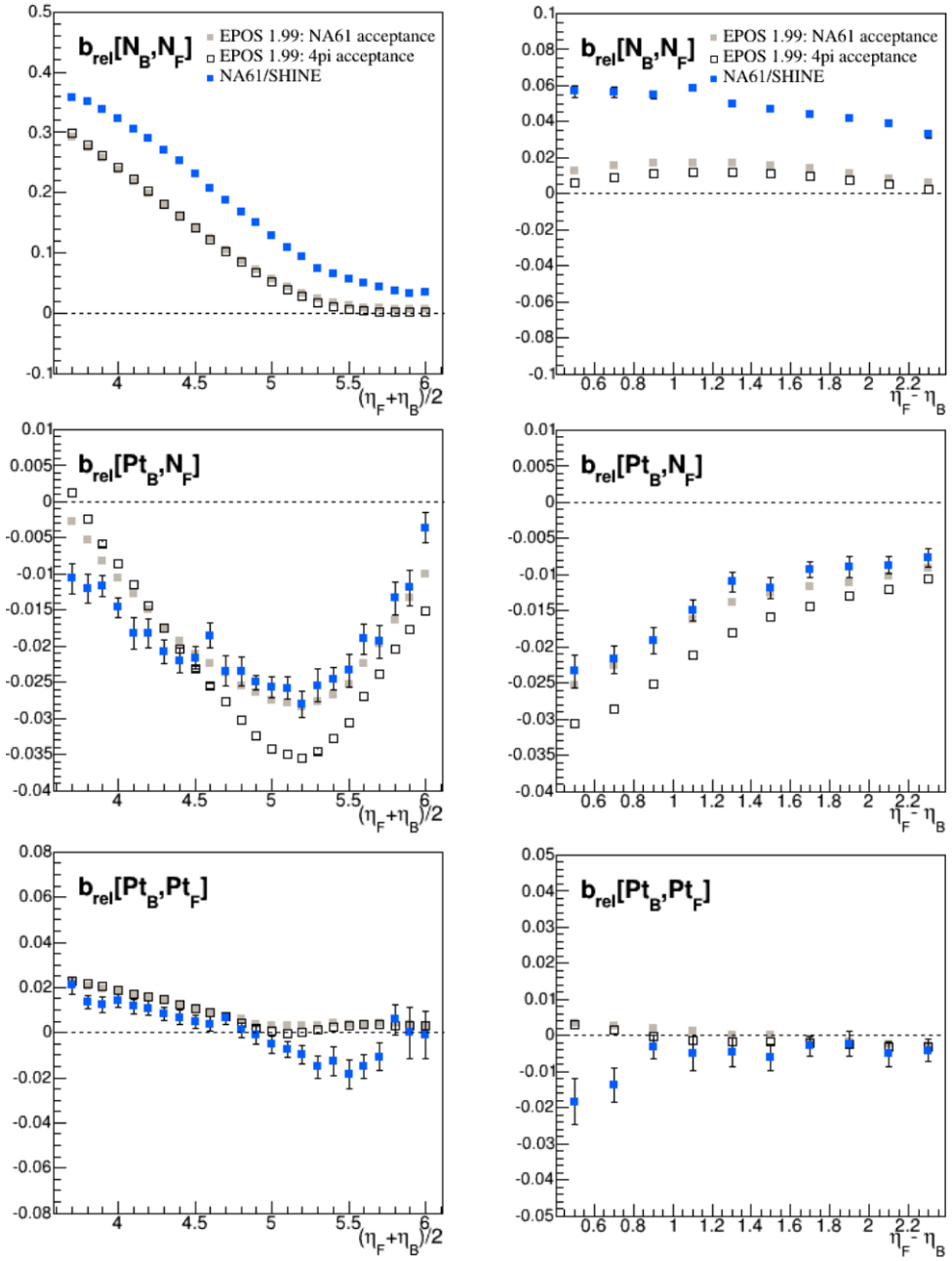

Figure 31: Pseudo-rapidity multiplicity and event mean transverse momenta correlation coefficient for Be+Be 150A GeV/c (full blue squares). *Left:* results obtained in short-range windows as a function of windows connection point (see Fig. 30). *Right:* results obtained in separated windows as a function of distance between windows (see Fig. 30). For comparison results from EPOS1.99 inside NA61/SHINE acceptance (open grey squares) and 4π-acceptance (open black squares) are shown.

exponential fit. The systematic uncertainty (shadow bands) is calculated as a square root of the sum of the squared measured systematic uncertainty and half of the extrapolated yield. Coloured lines correspond to the fits of sum of two identical Gaussian functions symmetrically displaced around mid-rapidity. This function describes the data well.

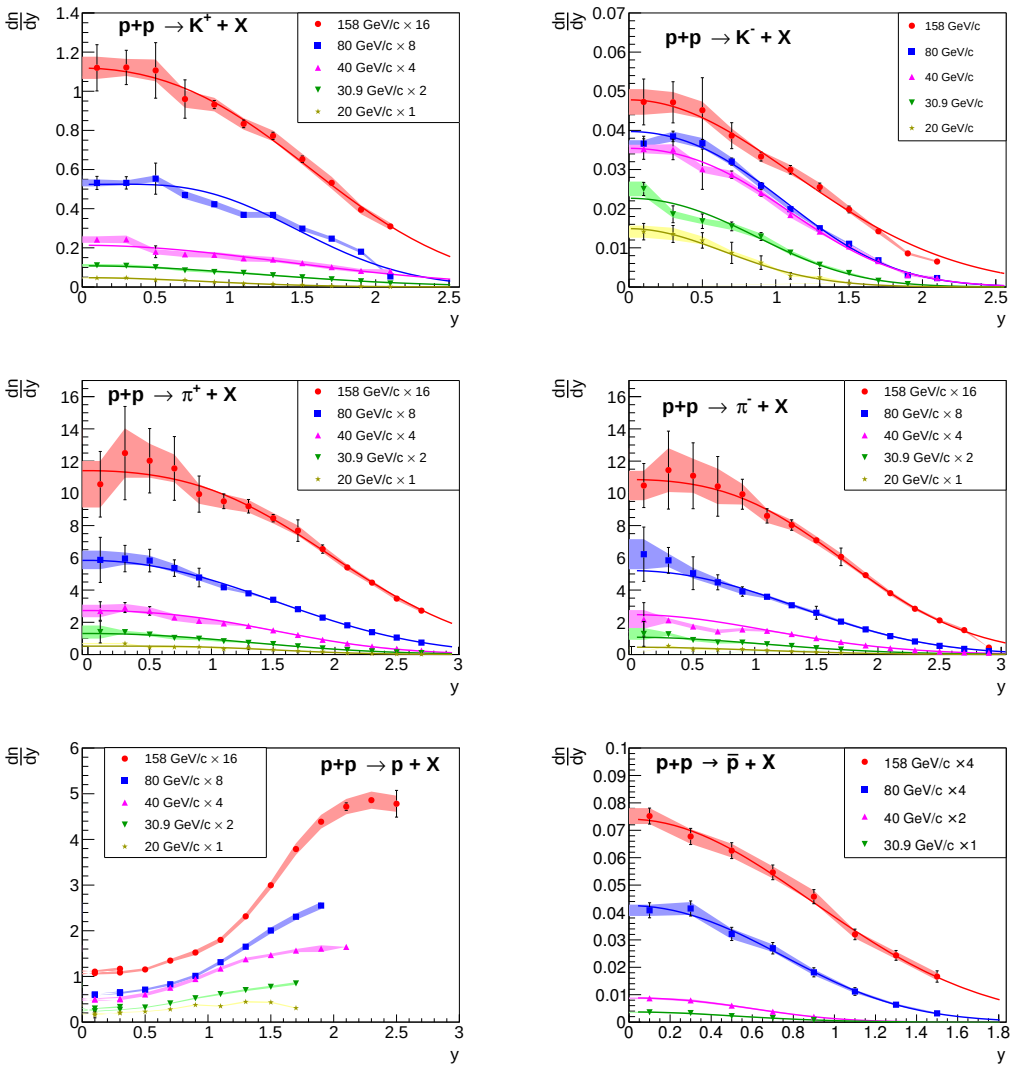

Figure 32: Rapidity spectra of $K^{\pm}$ (*top*), $\pi^{\pm}$ (*middle*), and $p/\overline{p}$ (*bottom*) at the SPS energy range, scaled by factors for visual separation.

Comparison of presented NA61/SHINE results, NA49 measurement and models: UrQMD [27, 28], EPOS [7] is presented in Fig. 33. The models do not describe well the high momentum (high rapidity) region for protons at 158 GeV/*c*.

The mean multiplicity of π^+, π^-, K^+, K^- and $\overline{p}$ were calculated as integrals of the double-Gaussian functions presented in Fig. 32. The mean multiplicities with the statis-

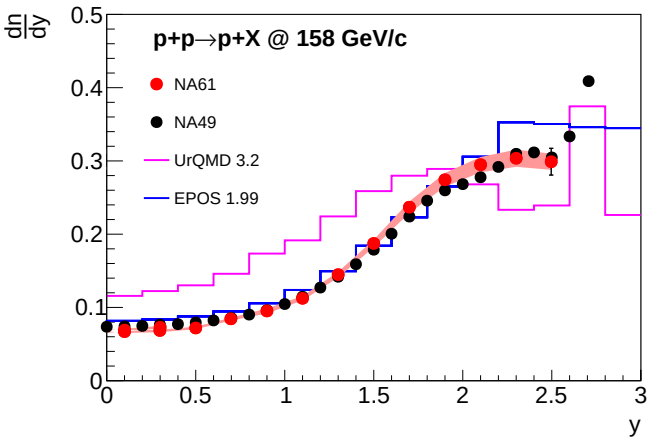

Figure 33: Proton rapidity distribution at 158 GeV/c compared with the NA49 measurement and Monte-Carlo models.

tical and systematical uncertainties are presented in Tables 2 and 3, for positively and negatively charged hadrons, respectively.

p_{beam} [GeV/c]	$\langle \text{K}^+ \rangle$	$\langle \pi^+ \rangle$
20	$0.097 \pm 0.014 \pm 0.0062$	$1.582 \pm 0.122 \pm 0.197$
30.9	$0.157 \pm 0.010 \pm 0.015$	$1.985 \pm 0.210 \pm 0.197$
40	$0.170 \pm 0.009 \pm 0.023$	$2.221 \pm 0.220 \pm 0.164$
80	$0.201 \pm 0.010 \pm 0.010$	$2.556 \pm 0.220 \pm 0.140$
158	$0.234 \pm 0.014 \pm 0.017$	$2.991 \pm 0.305 \pm 0.250$

Table 2: Mean multiplicity of positively charged hadrons at the SPS energy range with statistical and systematic uncertainties, respectively.

p_{beam} [GeV/c]	$\langle \text{K}^- \rangle$	$\langle \pi^- \rangle$	$\langle \bar{\text{p}} \rangle$
20	$0.024 \pm 0.006 \pm 0.002$	$1.067 \pm 0.053 \pm 0.196$	—
30.9	$0.045 \pm 0.004 \pm 0.003$	$1.438 \pm 0.219 \pm 0.187$	$0.0047 \pm 0.0007 \pm 0.0003$
40	$0.084 \pm 0.006 \pm 0.003$	$1.703 \pm 0.192 \pm 0.213$	$0.0059 \pm 0.0006 \pm 0.0004$
80	$0.095 \pm 0.004 \pm 0.005$	$2.030 \pm 0.248 \pm 0.132$	$0.0183 \pm 0.0015 \pm 0.0011$
158	$0.132 \pm 0.011 \pm 0.009$	$2.494 \pm 0.259 \pm 0.179$	$0.0402 \pm 0.0020 \pm 0.0026$

Table 3: Mean multiplicity of negatively charged hadrons at the SPS energy range with statistical and systematic uncertainties, respectively.

The mean multiplicity of charged kaons produced in inelastic p+p interactions is shown as a function of collision energy in Fig. 34. The NA61/SHINE results are presented together with the world data [29–37]. Most of the world data points come from bubble chambers experiments and they are presented here without the error bars (statistical uncertainty of 20–70%).

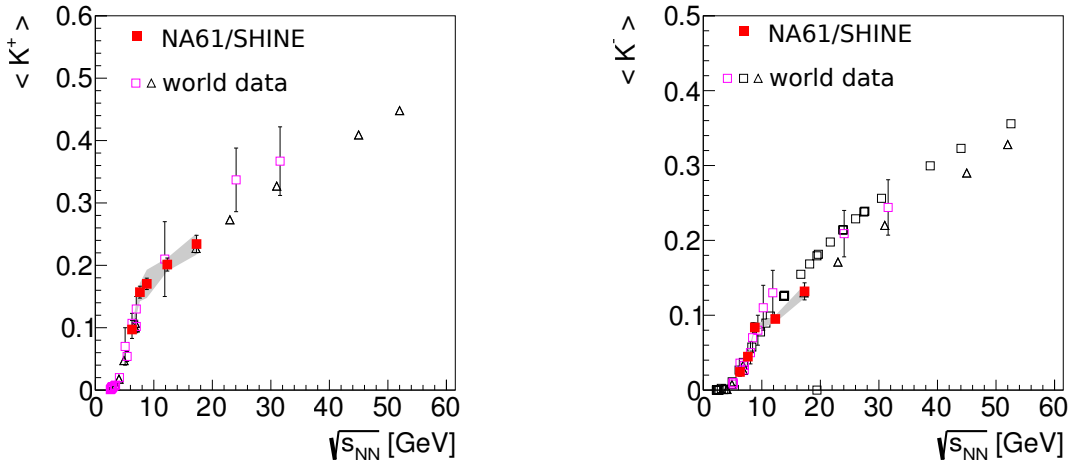

Figure 34: Mean multiplicity of charged kaons produced in inelastic p+p interactions as a function of collision energy. Statistical and systematical uncertainties of the NA61/SHINE measurements are presented by bars and shadow band, respectively. Black empty triangles represent the compilation of world data, fully corrected for the detector effects and feed-down [29]. The magenta open squares show data from compilation in Ref. [30]. Empty black squares are based on the parametrisation of the bubble chamber data with statistical error of 20–70% [32–37].

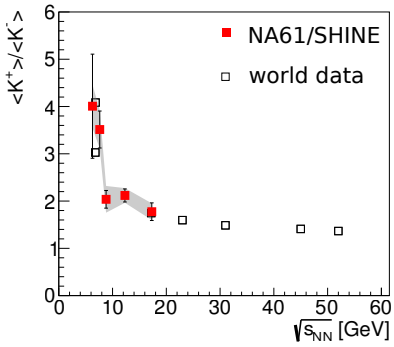

Figure 35: Ratio of mean multiplicities of positively and negatively charged kaons as a function of collision energy.

Figure 35 shows the ratio of mean multiplicities of positively and negatively charged kaons produced in p+p interactions together with the available world data [29]. The ratio decreases with the collision energy, and around 40 GeV/c ($\sqrt{s_{NN}} = 8.8$ GeV) reaches a constant value.

The collision energy dependence of mean multiplicity of negatively and positively charged pions is shown in Fig. 36. The multiplicities increase smoothly with the collision energy.

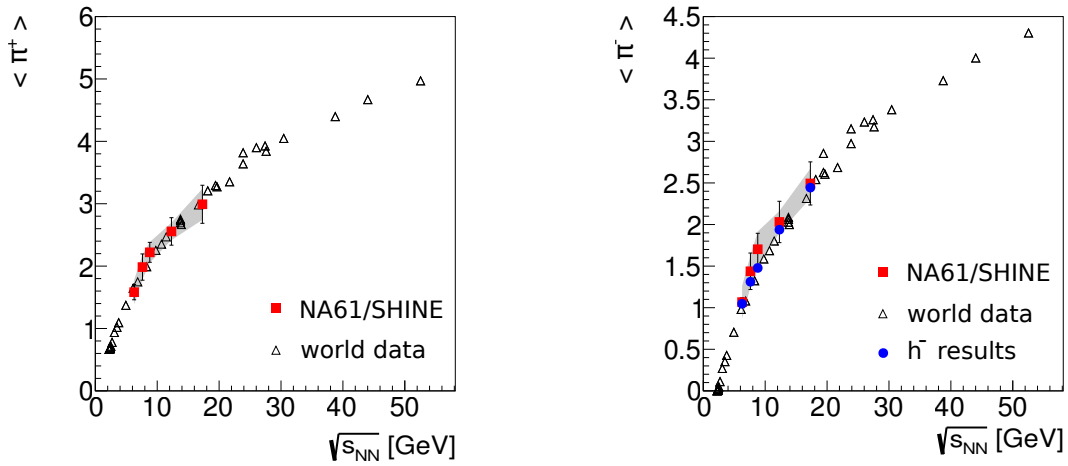

Figure 36: Mean pion multiplicity as the function of the collision energy. Black empty triangles represents the world data [38].

Figure 37 presents ratio of the mean multiplicities of charged pions. At the SPS energies, the ratio decreases slowly with the collision energy. The NA61/SHINE results agree with the data from other experiments.

Two-particle correlations in $\Delta\eta\Delta\phi$ in inelastic p+p interactions Two-particle correlations in $\Delta\eta$, $\Delta\phi$ were studied extensively at RHIC and LHC. They disentangle different sources of correlations: jets, flow, resonance decays, quantum statistics effects, conservation laws, etc. The preliminary results on two-particle $\Delta\eta\Delta\phi$ correlations in inelastic p+p interactions at the SPS beam momenta (20, 31, 40, 80, and 158 GeV/c) were presented in the previous report. Here, we will show the estimates of statistical and systematic uncertainties, as well as the new comparison of NA61/SHINE results with predictions of the UrQMD 3.4 model.

Correlations are calculated as a function of the difference in pseudo-rapidity ($\Delta\eta$) and azimuthal angle ($\Delta\phi$) between two particles in the same event:

$$\Delta\eta = |\eta_1 - \eta_2| \,, \qquad \Delta\phi = |\phi_1 - \phi_2| \,. \tag{11}$$

The $\Delta\phi$ range is folded, i.e. for $\Delta\phi$ larger than π its value is recalculated as $2\pi - \Delta\phi$.

The uncorrected ($^{\text{raw}}$) correlation function is calculated as:

$$C^{\text{raw}}(\Delta\eta, \Delta\phi) = \frac{S(\Delta\eta, \Delta\phi)}{N_{\text{signal}}} \Big/ \frac{M(\Delta\eta, \Delta\phi)}{N_{\text{mixed}}} \,, \tag{12}$$

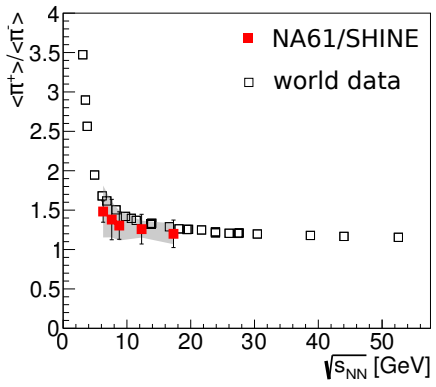

Figure 37: Ratio of the mean charged pion multiplicities in p+p interactions as a function of collision energy. World data is presented without uncertainties to increase readability.

where

$$S(\Delta\eta, \Delta\phi) = \frac{\mathrm{d}^2 N_{\mathrm{signal}}}{\mathrm{d}\Delta\eta\, \mathrm{d}\Delta\phi};\; M(\Delta\eta, \Delta\phi) = \frac{\mathrm{d}^2 N_{\mathrm{mixed}}}{\mathrm{d}\Delta\eta\, \mathrm{d}\Delta\phi} \tag{13}$$

are the distributions of particle pairs. S is calculated based on the measured events, while M on the mixed events. The mixing algorithm reproduces the number of measured (signal) events preserving the particles multiplicity in the events and filling them with particles with a constrain that any two particles in a new event cannot originate from the same measured event.

In order to allow for a comparison with the RHIC and LHC results the pseudorapidity was calculated in the centre-of-mass (CMS) system. The transformation from the laboratory system to the CMS was performed assuming the pion mass for all produced particles. Electrons and positrons were removed by a cut on $\mathrm{d}E/\mathrm{d}x$, the energy loss of the particle tracks in the TPC detectors.

In order to correct the measured raw correlation function for possible biases due to trigger and off-line event selection, track selection, etc. the same analysis was performed on simulated data. The bin-by-bin correction $\mathrm{Corr}(\Delta\eta, \Delta\phi)$ was calculated as the ratio of the correlation functions for generated events from the EPOS [7] model ($_{\mathrm{gen}}$) and the same events after processing through GEANT detector simulation and reconstruction ($_{\mathrm{rec}}$):

$$\mathrm{Corr}(\Delta\eta, \Delta\phi) = \frac{C^{\mathrm{MC}}_{\mathrm{gen}}(\Delta\eta, \Delta\phi)}{C^{\mathrm{MC}}_{\mathrm{rec}}(\Delta\eta, \Delta\phi)}\,, \tag{14}$$

where $C^{\mathrm{MC}}_{\mathrm{gen}}$ is the correlation function obtained for generated events and $C^{\mathrm{MC}}_{\mathrm{rec}}$ is the correlation function for these events after detector simulation and reconstruction. Both $C^{\mathrm{MC}}_{\mathrm{gen}}$ and $C^{\mathrm{MC}}_{\mathrm{rec}}$ were calculated within the NA61/SHINE acceptance.

Corrected correlation functions (for example in Fig. 38 (*right*)) were obtained by multiplying the uncorrected correlation function (Fig. 38 (*left*)) by the corresponding correc-

tions (Fig. 38 (*middle*)), namely:

$$C(\Delta\eta, \Delta\phi) = C^{\text{raw}}(\Delta\eta, \Delta\phi) \cdot \text{Corr}(\Delta\eta, \Delta\phi) \, . \tag{15}$$

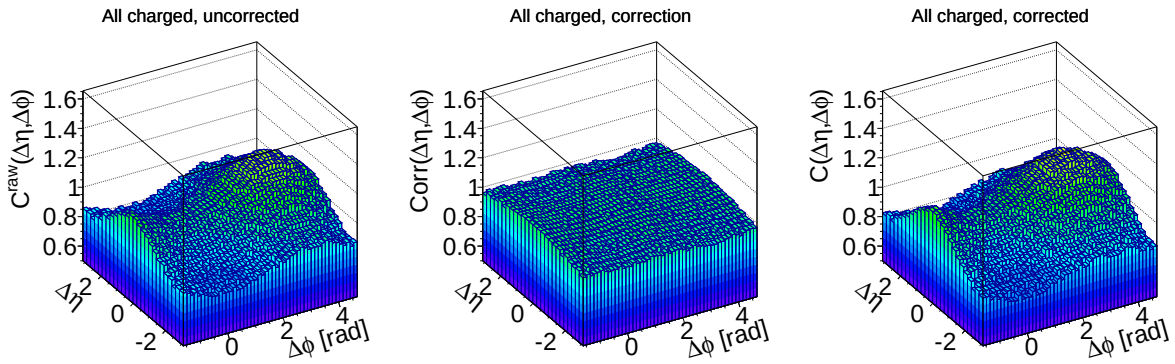

Figure 38: An example of the correction procedure for the correlation function in ineleastic p+p interactions at 80 GeV/c. *Left:* correlation function $C(\Delta\eta, \Delta\phi)$ for uncorrected data. *Middle:* bin-by-bin correction factors. *Right:* corrected correlation function.

Systematic uncertainties were estimated by varying event and track selection criteria. The calculations were performed for data at 20, 40 and 158 GeV/c. In this procedure the accuracy of the results on systematic uncertainties is limited by statistical errors. The upper limit of systematic uncertainties was estimated to be 1% with exception of the region $2 \leq \Delta\eta \leq 3$ at lower beam momenta where the upper limit of systematic uncertainty was 5%.

In the lower $\Delta\eta$ range ($0 \leq \Delta\eta \leq 2$) the systematic uncertainty dominates while in the upper range ($2 \leq \Delta\eta \leq 3$) the statistical uncertainty dominates. Statistical uncertainties rise with increasing $\Delta\eta$ from 0.5% for higher beam momenta of all charged combinations to 10% for negatively charged pairs of lower beam momenta.

The results for all charged particles is shown in Fig. 39. The maximum at $(\Delta\eta, \Delta\phi) = (0, \pi)$ is probably a result of resonance decays and momentum conservation.

Two-particle correlations can be also an unique tool to test models. Figure 40 shows qualitative agreement of the NA61/SHINE results with predictions of EPOS, whereas in URQMD the resonance peak at lower energies seems to be stronger than the observed values.

5.2 New results for neutrino physics

Long baseline neutrino experiments have constrained initial neutrino flux predictions using hadron production measurements. In short, interactions in Monte Carlo beam simulations are re-weighted according to measured hadron production rates.

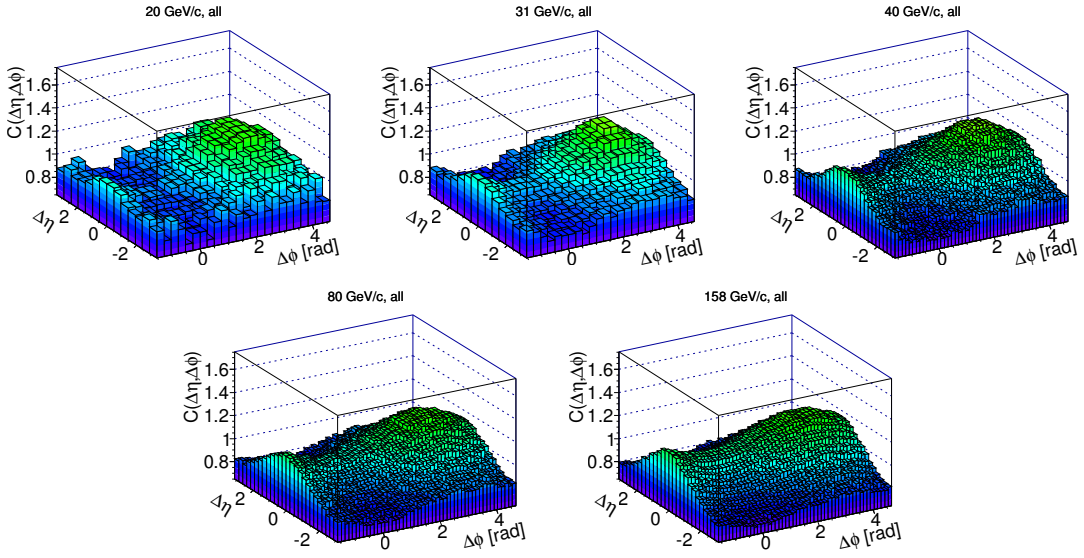

Figure 39: The results for $\Delta\eta\Delta\phi$ correlations for inelastic p+p interactions. The results for all charged particle pairs. The correlation function is mirrored around $(\Delta\eta, \Delta\phi) = (0, 0)$.

5.2.1 Results on p+C interactions at 31 GeV/c

Final results on the measurements of hadron production in p+C interactions at 31 GeV/c have recently been submitted for publication [39]. The analysis is based on the full set of data collected in 2009 using a graphite target with a thickness of 4% of a nuclear interaction length (the thin target). Inelastic and production cross sections as well as spectra of $\pi^{\pm}$, $K^{\pm}$, p, K^0_S and Λ have been measured with a high precision.

These measurements are crucial for predictions of the initial neutrino fluxes in the T2K long baseline neutrino oscillation experiment in Japan. Furthermore, they provide important input to improve hadron production models needed for the interpretation of air showers initiated by ultra high energy cosmic particles.

5.2.2 π^++C at 31 GeV/c: Interaction cross sections

A significant portion of the neutrinos in long baseline neutrino experiments is produced through pion re-interactions in the target and beam-line components. Tuning these pion interactions can supplement the tuning of the primary interaction and lead to a further reduction on the uncertainty of the neutrino flux prediction.

During the 2009 p+C at 31 GeV/c thin target data taking, a secondary trigger (T4) recorded interactions of beam pions, kaons and protons. Though the purpose of this trigger was to do beam studies, it can be exploited to study pion interactions. The statistics are enough to make a measurement of the production and inelastic cross sections and measure the multiplicities of charged pions. The beam momentum of 31 GeV/c is in the right range to tune pion re-interactions for Fermilab neutrino experiments.

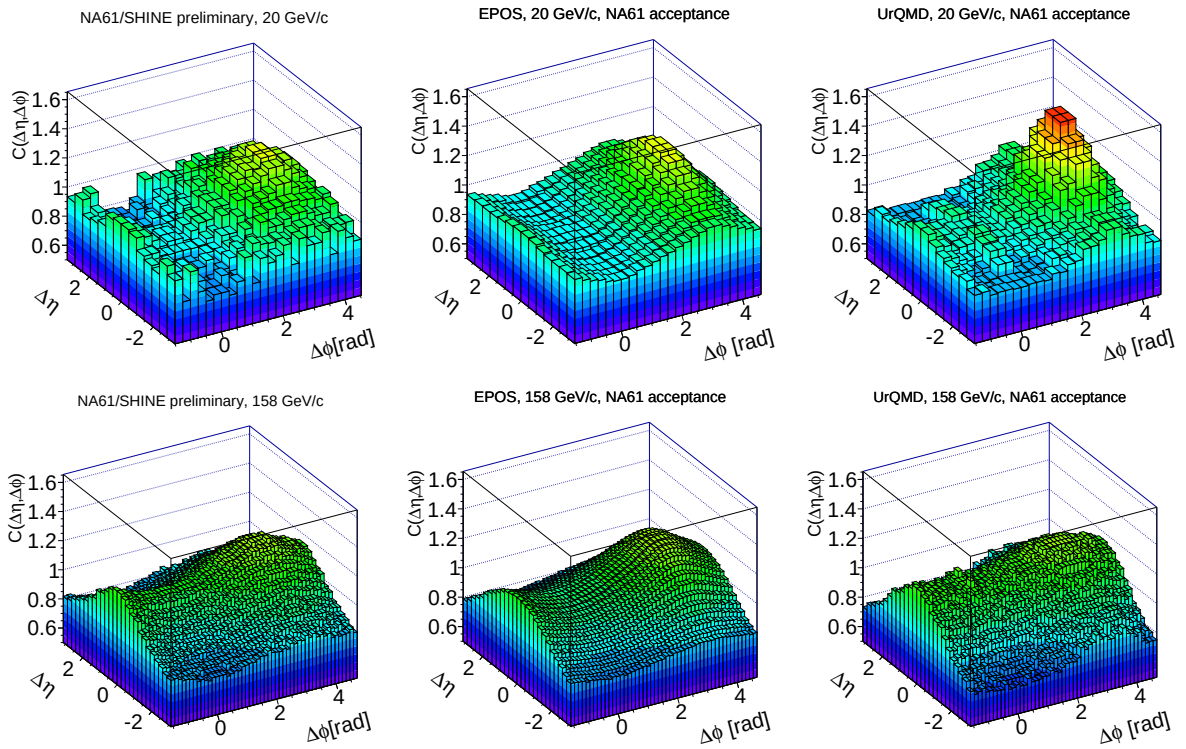

Figure 40: A comparison of $\Delta\eta\Delta\phi$ correlations in inelastic p+p collisions measured by NA61/SHINE with models (EPOS 1.99 and URQMD 3.4). Results concern all charged particles in the NA61/SHINE acceptance.

The analysis of this dataset is under-way. Preliminary results has been obtained for the production and inelastic cross sections:

$$\sigma_{\text{prod}} = 197.2 \text{ mb} \pm 3.1(\text{stat})^{+2.5}_{-0.0}(\text{model}) \,, \tag{16}$$

$$\sigma_{\text{inel}} = 212.5 \text{ mb} \pm 3.1(\text{stat})^{+0.7}_{-0.0}(\text{model}) \,. \tag{17}$$

The evaluation of the systematic uncertainty is not yet complete, so it is not shown. At this stage of the analysis, the leading contributions to the systematic uncertainty appear to be the uncertainty on the elastic cross section and the uncertainty on the beam composition. After the normalization analysis is completed, multiplicity spectra of charged pions will be analyzed.

5.2.3 Results on p+(T2K Replica Target) at 31 GeV/c

The hadron production measurements are intended for improving predictions of the initial neutrino flux in the T2K long-baseline neutrino oscillation experiment at J-PARC, Japan. A detailed knowledge on the charged pion differential yields from the surface of the T2K replica target is necessary to improve the accuracy of the neutrino flux predictions.

Analysis of the 2009 dataset The hadron spectra in interactions of a proton beam with T2K replica target were derived using three analysis methods.

In the first method, called the *tof*-dE/dx method, the $\pi^{\pm}$ are identified based on *tof* and dE/dx measurements. These results [40] will be submitted for publication soon and therefore are not discussed in detail here.

Results from the h^- analysis The second method use the so-called h^- analysis. It allows the derivation of spectra of primary and secondary particles generated in the target and covers the largest accessible phase space region. Models and experimental findings show that the negatively-charged particles produced by 31 GeV/c protons bombarding C target consist mainly Models and experimental findings show that the negatively charged hadrons produced in p+C interactions at 31 GeV/c consist mainly of π^-, with a small admixture of K^- and a negligible fraction of $\overline{p}$. Hence the h^- method allows for differential yields of π^- mesons in the full momentum range, see Ref. [41]. Since the kaon contamination is small it can be removed by Monte Carlo corrections without bringing large systematic biases. Furthermore, as pions and electrons are well separated in the dE/dx distributions, this analysis does not require the *tof* information.

Once the h^- tracks were selected, a fit to the dE/dx distributions was performed to precisely separate h^- and e^- from the sample of negatively-charged particles. Then the h^- analysis proceeded into two branches which differ by methods to apply the Monte Carlo corrections: the standard weight method and an unfolding approach.

In the weight method, the Monte Carlo corrections were calculated and applied to the data as weights on a bin-by-bin basis resulting in the differential π^- yields. This weight method of correcting the data is also used in the *tof*-dE/dx analysis.

In the unfolding method, the extracted set of h^- tracks was processed by an unfolding technique. This method reduces systematic uncertainty related to a proper modelling of the interaction process in the Monte Carlo simulation. The unfolding was performed within the RooUnfold framework [42]. The RooUnfold package provides several deconvolution algorithms. The one used in the analysis is the iterative "Bayesian" proposed by D'Agostini [43]. This algorithm consists of the repeated application of Bayes' theorem to invert the response matrix.

The results on π^- spectra from the *tof*-dE/dx, h^- weight and h^- unfolding methods are compared in Fig. 41.

The π^- differential yields computed with the unfolding technique are in good agreement with those obtained by the *tof*-dE/dx approach. Some small deviations appear only in the upstream target region for the polar angle bin $0 < \theta < 20$ mrad and low momentum (6–7 GeV/c in average but not higher than 10 GeV/c), where the unfolded yields exceed those obtained with the *tof*-dE/dx approach by a few percent, actually remaining slightly outside of the estimated error bars, as seen in Fig. 41.

The unfolding algorithm extracts a set of tracks, that do not fit the analysis requirements. These tracks are called fake. A reconstructed track is treated as fake if: i) it does not have a MC match, ii) it has a MC match but does not come from the target and iii)

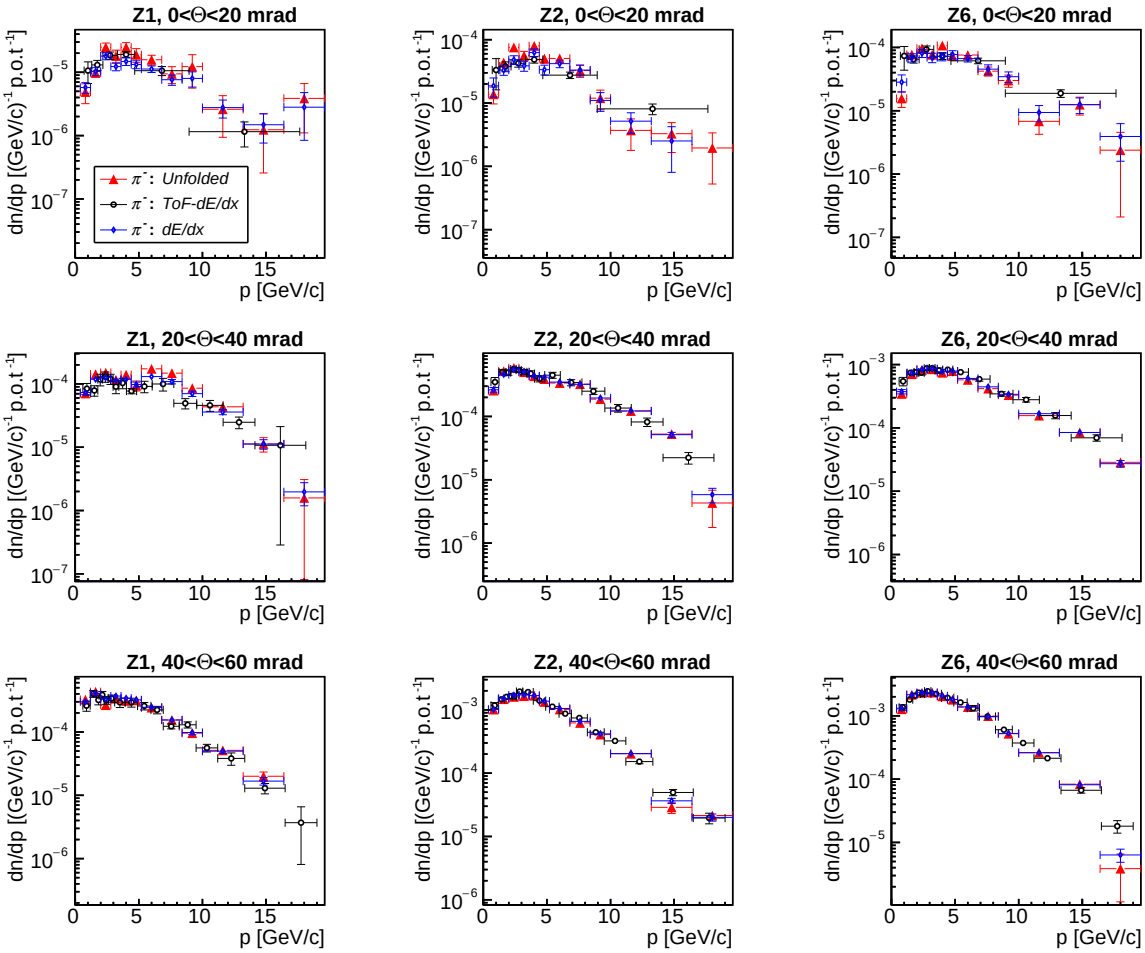

Figure 41: Differential yields of π^- mesons produced in p+(T2K Replica Target) at 31 GeV/c obtained using different analysis techniques. The upstream target region (Z1 and Z2 target bins, *left* and *middle*) is displayed together with the most downstream bin Z6 (downstream target face, *right*). The error bars present statistical uncertainties for results from h^- weight and *tof*-dE/dx methods and the full uncertainties for the h^- unfolded method. Good agreement is observed, except for the first angular interval in the upstream part of the target.

is a track of a negatively-charged particle with a MC match that can not be identified as an electron or pion. Some further information can be found in Ref. [42]. In the p–θ and Z bins considered above the relative number of fake tracks is the highest. For the very first target bin (Z1) and momentum below 6 GeV/c this number is about 50% on average but decreases to less than 10% for the rest of momentum bins. For all other longitudinal target bins the relative number of fakes for all p–θ bins is below 5%. Thus higher π^- yields arise in the bins where the statistical abundance is poor and relative number of

fake tracks is the highest. In the other p–θ bins a good agreement between unfolding and other analysis techniques is observed.

Systematic uncertainties determined by unfolding for the h^- analysis. For the differential yields of π^- computed by means of the *tof*-dE/dx and dE/dx methods a comprehensive specification of the dominant sources of systematic uncertainties is available in Ref. [40]. An estimate of the systematic uncertainties for the differential yields obtained with the unfolding technique was obtained assuming that the appearance of fake tracks reflects an integrated effect of the contributions from the sources enumerated in Ref. [40]. The magnitude of the systematic uncertainties in a given p–θ bin was measured by the relative content of the fake tracks in that bin. The uncertainties obtained by unfolding were used for a cross-check with those produced by a detailed study of every individual source. It is considered that the systematic uncertainties from both approaches are in good agreement and remain on average around 3–4% or less per longitudinal target bin, see Fig. 42. The total error, defined as a sum of statistical and systematic uncertainties, shows an average value of about 7% for each longitudinal target bin.

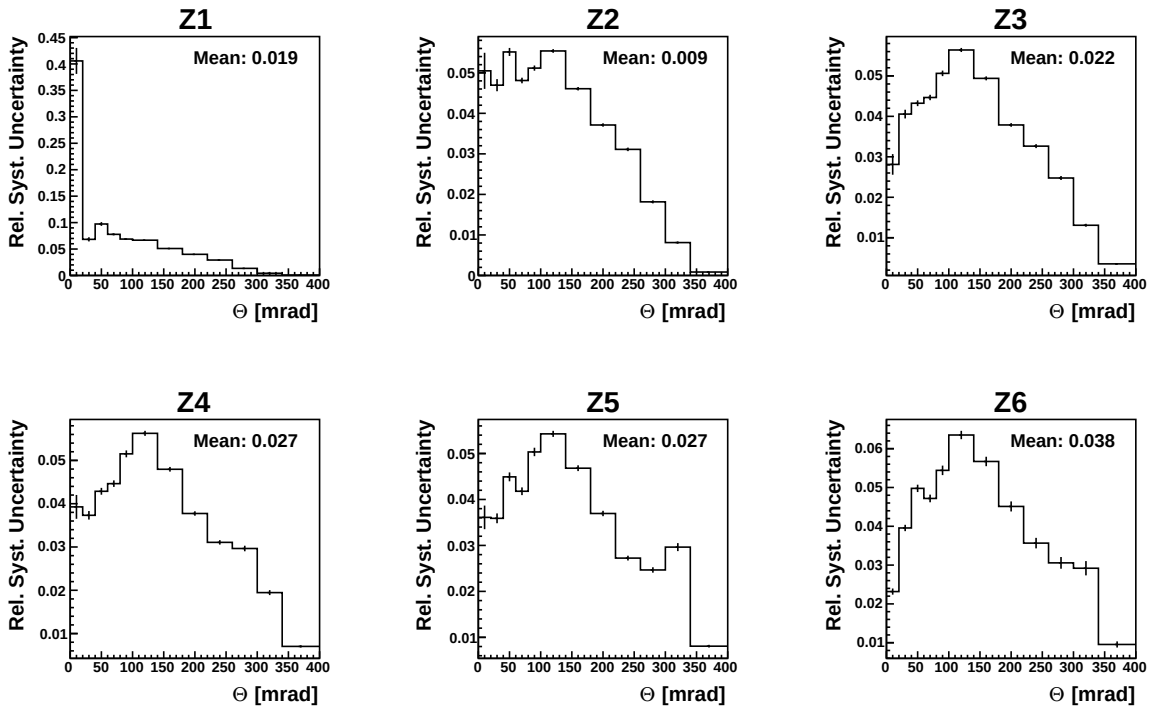

Figure 42: The h^- relative systematic uncertainties for polar angles from 0 to 400 mrad in the longitudinal target bins. The weighted mean uncertainties are shown at the upper left corners of the graphs.

Analysis of the 2010 dataset Since the last status report [8], analysis of high-statistics dataset recorded in 2010 has been started. The 2010 dataset consists of 10.2 million events, 1.2 million of which were recorded with the 158 GeV/c magnetic field configuration in order to cover the forward region of phase space ($\theta < 50$ mrad). Pions from this region of phase space are the main source of high-energy muons. In long-baseline neutrino experiments such as T2K, monitoring of the production and direction of high-energy muons is important since it is directly correlated with the neutrino beam intensity and direction.

Analysis of 2010 dataset is the first analysis of p+(T2K Replica Target) events done in SHINE analysis framework. Major technical issue was adapting FLUKA and GEANT3 simulation based on legacy software and converting its output to SHOE format. This problem has been recently solved by slightly changing output of the simulation. With exception of the differences in the framework used, the analysis procedure is the same as for the 2009 dataset. Particles are identified via combined *tof* and dE/dx measurement.

In analysis of the 2009 dataset, a major systematic uncertainty is coming from track extrapolation in the magnetic field which is due to uncertainty of the target position with respect to the TPCs. This problem has been extensively studied in this analysis in order to significantly improve the results. Target x and y position with respect to the beam can be obtained by calculating centre of x–y distribution of beam particles in T2 events. Target position calculated this way can be used only if the beam and TPCs are perfectly aligned. It has been shown that beam-TPC alignment procedure used for thin target cannot be correctly applied for T2K replica target. Whole procedure has been modified in order to avoid multiple scattering inside the target.

First, target alignment with respect to the TPCs is calculated by using a procedure developed for analysis of 2007 dataset. It has been found that the target is perfectly aligned with precision of 0.1 mrad. Then, events with beam particles hitting the outside layer of the target are chosen in order to minimize scattering inside the target.

TPC tracks are extrapolated towards the beam tracks and the target z position is calculated from the z distribution of the points of closest approach. When the z position of the target is known, it is possible to consider tracks extrapolated to the most downstream, 2 cm-thick section of the target. In this way the extrapolated path through the carbon is minimized and strict cuts on the extrapolation quality ensure that the track is not produced in a secondary interaction. Now, the beam-TPC alignment procedure for thin target can be used. It has been found that the error of the above described beam-TPC alignment is around 30 μm for the x direction and 60 μm for the y direction, which is considerably better than in 2009. Finally, the target x and y position with respect to the beam is calculated and corrected for beam-TPC misalignment.

$$(x,\ y,\ z) = (-0.096,\ 0.233,\ -657.400)\ \text{cm}\ . \tag{18}$$

$$(\delta x,\ \delta y,\ \delta z) = (0.011,\ 0.005,\ 0.050)\ \text{cm}\ . \tag{19}$$

Besides reducing systematics, the correct target position is needed for the production of Monte Carlo dataset. Various other studies have been preformed. Quality cuts have

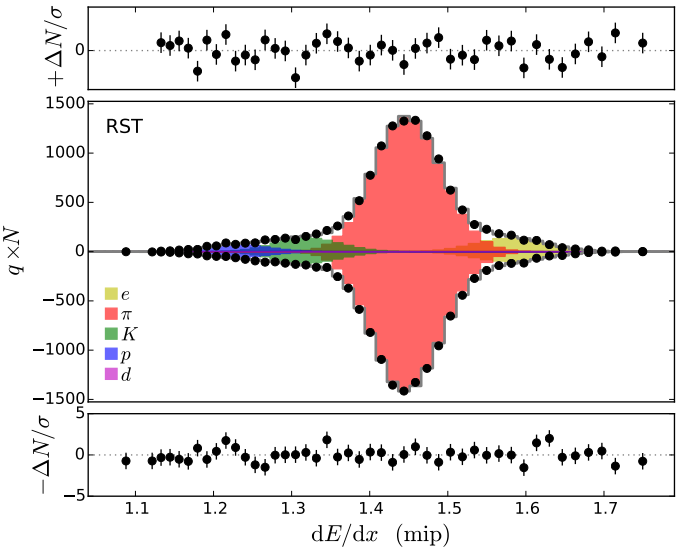

Figure 43: Example of a $\mathrm{d}E/\mathrm{d}x$ fit ($\langle p \rangle = 28.4\,\mathrm{GeV}/c$, $0 < p_\mathrm{T} < 0.1\,\mathrm{GeV}/c$). The middle panel shows the energy deposit of positively and negatively charged tracks. The fitted particles are indicated by colored histograms. Residuals to the fit are shown in the upper and lower panels.

been tuned in order to increase acceptance and to reduce errors. In the next report, preliminary multiplicities of pions are expected.

5.3 New results for cosmic-ray physics

A preliminary release of the spectra of charged pions in π^-+C interactions at 158 and 350 GeV/c and the spectra of ρ^0 mesons at 158 GeV/c was made in 2015 for the 34th International Cosmic Ray Conference [44].

5.3.1 Identified Hadron Spectra

For each track detected in the TPCs of NA61/SHINE, the particle type can be estimated by using the truncated mean of the energy that is deposited per unit track length ($\mathrm{d}E/\mathrm{d}x$) along the particle trajectory. An example of a $\mathrm{d}E/\mathrm{d}x$-distribution in a specific bin in momentum p and transverse momentum p_T is shown in Fig. 43. As can be seen, the distribution can be well described by the sum of the energy loss distributions of electrons, protons, pions and kaons (see Ref. [45] for details) and given the fitted fraction of each particle type, the corresponding number, Δn, of produced tracks within each p/p_T-bin can be reconstructed.

This number is then corrected for the detector acceptance, selection efficiency, feed-down from weak decays and re-interactions in the target. The latter two corrections are estimated using hadronic event generators (EPOS1.99, QGSJETII-04, DPMJET3.06) and they are typically well below 5%, but can reach up to 20% at low particle momenta. Overall, the systematic uncertainty of the corrected number of tracks, Δn, is estimated to be $\leq$7%.

The average multiplicity of particles produced within a p/p_T-bin is then obtained by dividing Δn by the total number of events in which an interaction occurred, N_prod.

N_{prod} is estimated by extrapolating the number of recorded interaction triggers to full phase space. The correction amounts to $(92.5 \pm 3.5)\%$ at 158 GeV/c and $(92.5 \pm 4.0)\%$ at 350 GeV/c, where the uncertainty was derived by running different generators to evaluate the correction.

The measured average multiplicities of charged pions are shown in Fig. 44 and the measurements are compared to predictions of pion production in π^-+C at 158 GeV/c from hadronic interaction models in Fig. 45. As can be seen, none of the generators describes the data well.

5.3.2 Resonances

The measurement of resonances in π+C is useful to constrain the production of ρ^0 meson, which is important to predict the number of muons observed in air showers (see e.g. Ref. [50]).

In the inclusive $\pi^+\pi^-$ invariant mass spectra there is a large combinatorial background, which dominates over the signal distributions of individual resonances. The method used to estimate the background is the so called charge mixing, which uses the $(\pi^+\pi^+ + \pi^-\pi^-)$ mass spectra as an estimate of the background.

The fitting procedure uses templates of the $\pi^+\pi^-$ mass distribution for each resonance. These templates are constructed by passing simulated π+C interactions, generated with the EPOS1.99 [51] hadronic interaction model using CRMC v1.5.3 [52], through the full NA61 detector Monte Carlo chain. All the cuts that are applied to the data are also applied to the templates. This method of using templates allows for the fitting of both resonances with dominant three body decays, such as the ω, and resonances with non-$\pi^+\pi^-$ decays, such as the K^{*0}. The data is split into bins of Feynman-x, x_F.

The fit to the $\pi^+\pi^-$ mass spectrum is performed between masses of 0.4 GeV/c and 1.5 GeV/c using the expression

$$F(m) = \sum_i \beta_i \, T_i(m) \, ,$$

where β_i is the relative contribution for each template, T_i, used. An example of one of these fits can be seen in Fig. 46. The templates in the fit are the background found from charge mixing and the following resonances: ρ^0, K^{*0}, ω, f_2, f_0 (980), a_2, η and K^0_S.

The fitting method is validated by applying the same procedure to the simulated data set which was used to construct the templates for the fit. For the majority of x_F bins there is good agreement between the fit and the true value, with some discrepancies for larger x_F bins of up to 20%. This bias is corrected for in the final analysis. The data is also corrected for losses due to the acceptance of the detector, as well as any bias due to the cuts used and any reconstruction inefficiencies. Apart from the acceptance, these corrections are typically less than 20%.

The average multiplicity of ρ^0 mesons is presented in Fig. 47. Also shown are predictions by EPOS1.99 [51], DPMJET3.06 [49], SIBYLL2.1 [47], QGSJETII-04 [48] and EPOSLHC [46]. It can be seen that there is an underestimation of the ρ^0 yield for almost

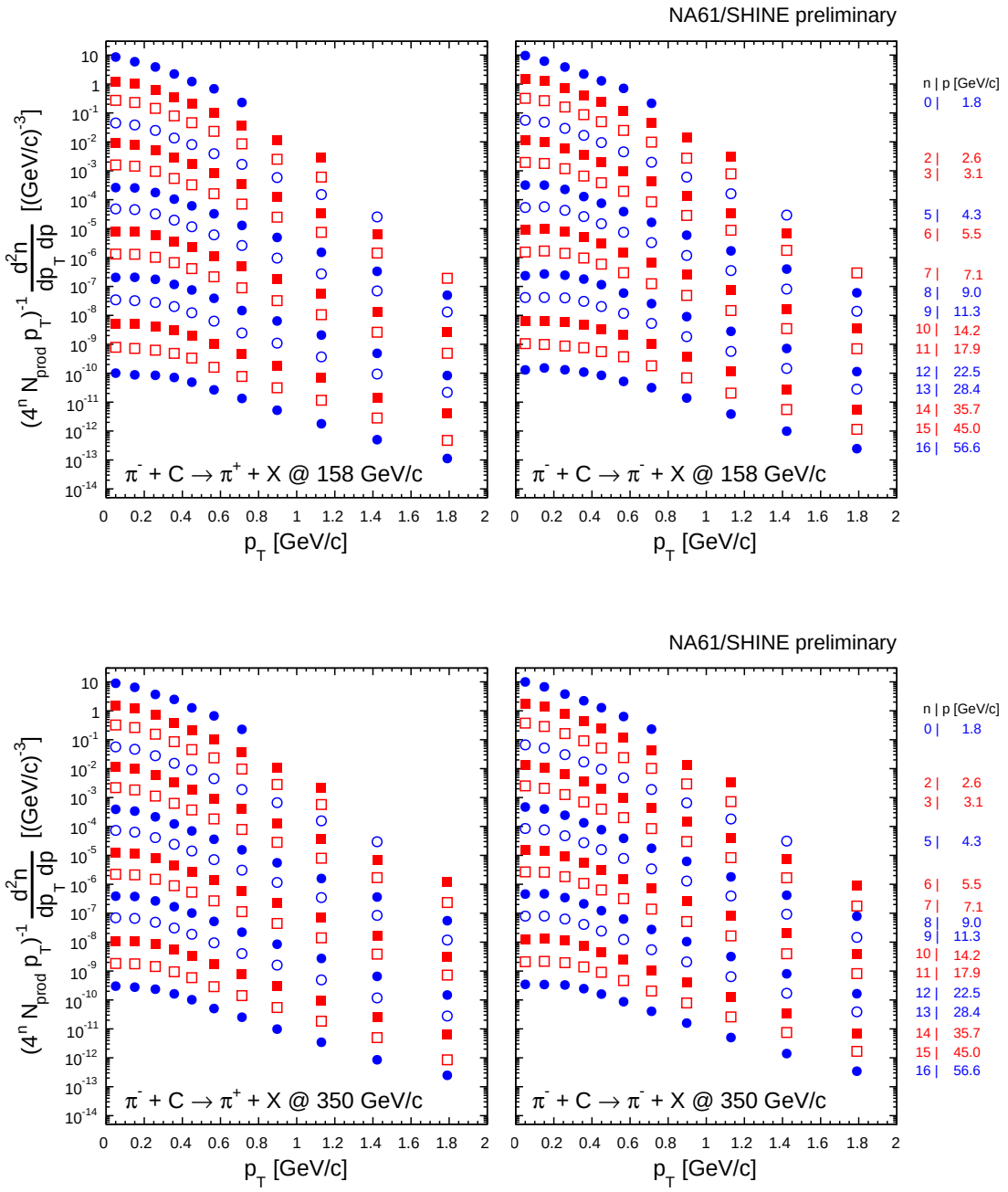

Figure 44: Inclusive spectra of charged pions in π^-+C interactions at beam energies of 158 (*top*) and 350 GeV/*c* (*bottom*). For better visibility, the spectra from the nth momentum bin are multiplied by a factor of $1/4^n$. The momentum increases from top to bottom as indicated in the legend on the right.

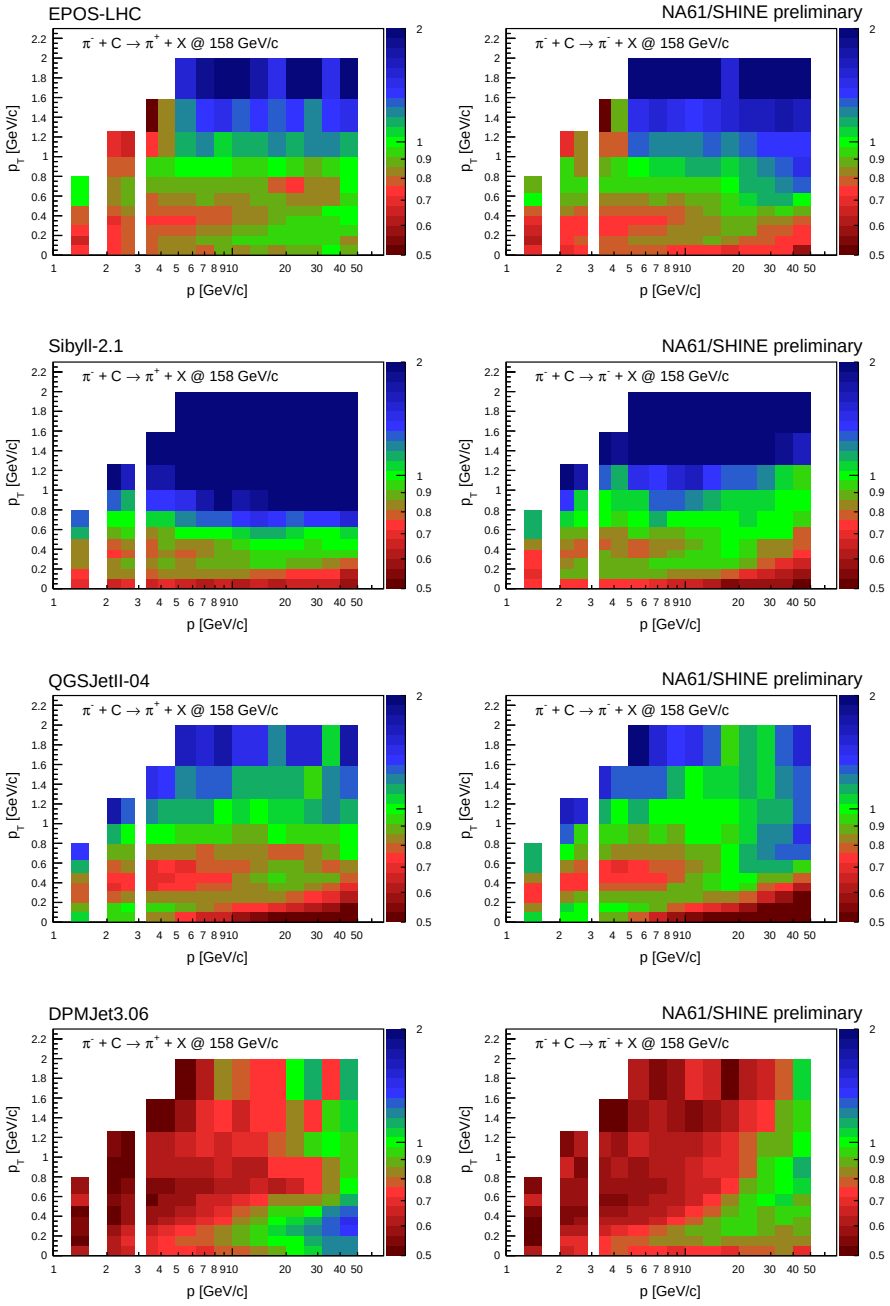

Figure 45: Comparison of the measured production spectra of charged pions to predictions from hadronic interaction models used for the interpretation of cosmic ray data [46–49]. The colours denote the ratio of data to simulation and the colour scale is truncated at 0.5 and 2. The two empty p-bins at $p \lesssim 2\,\text{GeV}/c$ and $p \gtrsim 3\,\text{GeV}/c$ are momenta excluded from the analysis due to the ambiguity with the energy deposit distributions of other particles types.

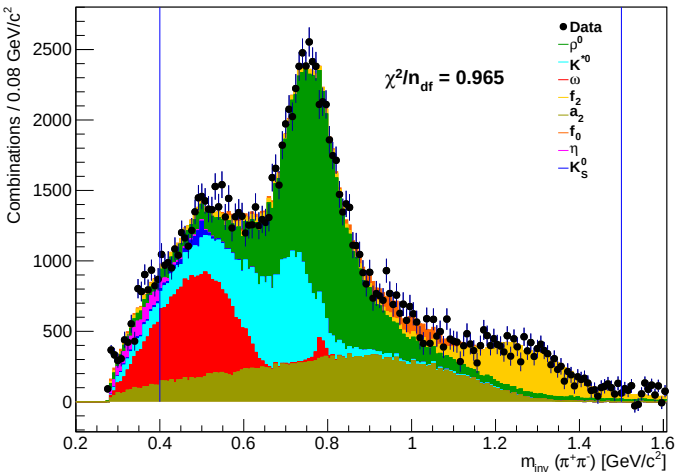

Figure 46: $\pi^+\pi^-$ invariant mass distribution in π^-+C interactions at 158 GeV/c in the range $0.4 < x_F < 0.5$. Dots with error bars denote the data and the fitted resonance templates are shown as filled histograms. The vertical lines indicate the range of the fit.

all hadronic interaction models, with the exception of QGSJETII-04 for $x_F > 0.8$. It is interesting to note that while QGSJETII-04 and EPOSLHC were tuned to NA22 π^++p data [53], there is an underestimation in π^-+C.

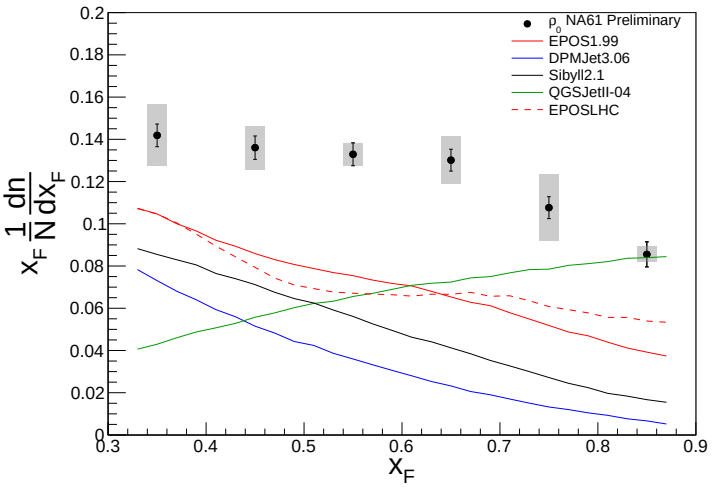

Figure 47: Average multiplicity of the ρ^0 meson in π+C at $p_{\text{beam}} = 158$ GeV/c as a function of Feynman-x. The bars show the statistical statistical uncertainties; the bands indicate systematic uncertainties. The lines are predictions of hadronic interaction models: red – EPOS1.99, blue – DPMJET3.06, black – SIBYLL2.1, green – QGSJETII-04, dashed red – EPOSLHC.

The systematic uncertainties are estimated by comparing correction factors for different hadronic interaction models (EPOS and DPMJET), by applying the bias-correction using different background estimates and by varying the cuts applied to the data. The systematic uncertainty is dominated by the background subtraction, up to 14%, whereas

the other uncertainties are less than 4%. Other sources of uncertainty, such as using templates from a different model, are found to be significantly smaller.

6 Data-taking plan: 2016–2018

The revised NA61/SHINE data-taking plan is presented in Table 4. Following the current accelerator schedule the plan assumes that the data-taking with a primary Xe beam will take place in 2017 and with a Pb beam in 2016 and 2018. It is also assumed that hadron beams will be available for several months each year until the Long Shutdown 2.

Beam		Target	Momentum	Year	Days	Physics
Primary	Secondary		(A GeV/c)			
p			400			
	h^+	A	40-400	2016	4x7 days	installation/tests
p			400			
	p	p	400	2016	28 days	SI
p			400			
	h^+	A	30–120	2016	42 days	ν
Pb		Pb	13, 19, 30, 40	2016	40 days	SI
Pb		Pb	150	2016	5 days	installation/tests
p			400			
	p	p/Pb	13, 19, 30, 40, 75	2017	35 days	SI
p			400			
	h^+	A	30–120	2017	42 days	ν
Xe		La	13, 19, 30, 40, 75, 150	2017	60 days	SI
p			400			
	p	p/Pb	13, 19, 30, 40, 75	2018	35 days	SI
p			400			
	h^+	A	30–120	2018	42 days	ν
Pb		Pb	75, 150	2018	40 days	SI

Table 4: The NA61/SHINE data taking plan revised in 2015. The following abbreviations are used for the physics goals: SI – measurements for physics of strong interactions, ν – measurements for the Fermilab neutrino beams.

Figure 48 schematically illustrates the status and plans for data-taking within the NA61/SHINE (beam momentum)-(system size) scan.

The 2016 beam request is explained as follows:

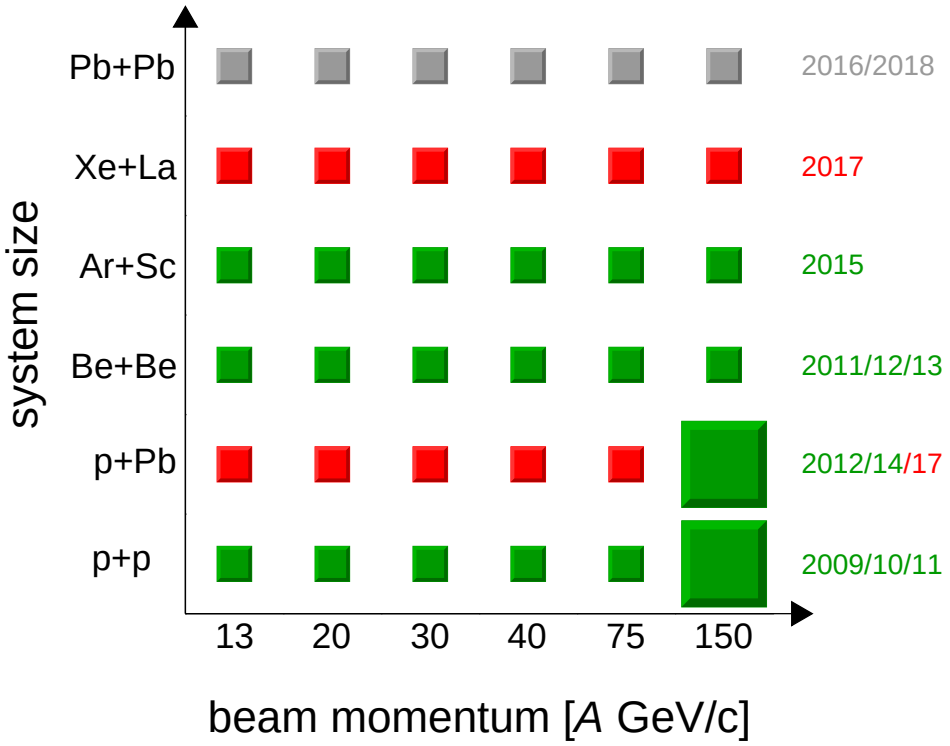

Figure 48: The NA61/SHINE data taking schedule for the (beam momentum)-(system size) scan and its proposed extension for the period 2016–2018 (in gray).

1. 28 days of h^+ beam at 400 GeV/c are needed for the installation and testing of the facility upgrades: Forward-TPCs, Vertex Detector, SciFi Beam Detectors, PSD and DRS4 read-out.

2. 28 days of proton beam at 400 GeV/c are needed for data-taking on p+p interactions.

3. 42 days of h^+ beam at 30–120 GeV/c are needed for data-taking for the Fermilab neutrino beams.

4. 60 days of Pb beam at 13A, 19A, 30A and 40A GeV/c are needed for data-taking on Pb+Pb collisions. This first part of the Pb+Pb beam momentum scan will be completed in 2018.

5. 5 days of Pb beam at 150A GeV/c is needed for pilot data taking with the Vertex Detector and the ultimate test of the PSD performance.

7 Proposals to extend the NA61/SHINE physics programme

This section summarizes the NA61/SHINE plans to extend its physics programme.

First, following arguments presented in Ref. [54], the Collaboration considers performing the full energy scan with Pb+Pb collisions. Data taking at the low SPS beam momenta, 13A, 19A, 30A and 40A GeV/c shall take place in 2016, with runs at higher beam momenta, 75A GeV/c and 150A GeV/c, in 2018. The physics motivation of this proposal is twofold:

(i) The new data in the full SPS energy range will allow for the study of the collisional energy dependence of collective effects in non-central Pb+Pb collisions via measurements of hadron correlations in azimuthal angle. This may lead to a new insight into the origin of rapid changes of hadron production properties at the SPS energies which are interpreted as due to the onset of deconfinement.

(ii) The data at the two top SPS energies recorded after the new Vertex Detector is constructed and installed will lead to the first direct measurements of open charm production in heavy ion collisions at the SPS.

The proposal is presented in detail in a separate document (Addendum to the NA61/SHINE proposal) [55] submitted to the SPSC in parallel with this Status Report.

Secondly, NA61/SHINE plans to continue measurements of hadron production properties in hadron-proton, hadron-nucleus and nucleus-nucleus collisions at the CERN SPS after the Long Shutdown 2. The following suggestions are under discussion:

(i) Precise measurements of open charm and multi-strange hyperon production with the large acceptance Vertex Detector and increased data taking rate. This would require a significant upgrade of the NA61/SHINE read-out electronics and DAQ system.

(ii) Systematic measurements of hadron production in proton-nucleus and antiproton-nucleus interactions to study mechanisms of particle production and propagation in cold nuclear matter. In particular, a better understanding of collective/cumulative effects is of high interest.

(iii) Measurements of event-by-event fluctuations of charged hadron properties in the full phase space. This would require a significant upgrade of the NA61/SHINE tracking system.

(iv) Precise measurements of hadron production cross sections needed for cosmic ray studies, in particular for the AMS experiment. This would possibly require a new electro-magnetic calorimeter.

(v) Precise measurements of hadron emission from replica targets of the neutrino beam facilities at Fermilab and J-PARC. This would require the addition of a high precision tracking detector located close to the replica targets.

8 Summary

This report presented briefly the status and plans of the NA61/SHINE experiment [1] at the CERN SPS.

The summary of this report is as follows:

(i) Recorded data (see Section 2): After the Long Shutdown 1 data-taking within the approved programme continued with runs on p+Pb interactions at 158 GeV/c in November–December 2014. The beam momentum scan with Ar+Sc collisions was successfully executed in February–April 2015. Due to the failure of the VERTEX-1 magnet the physics data taking for p+p interactions at 400 GeV/c, for the Fermilab neutrino beams and for Pb+Pb collisions at 30A GeV/c was cancelled. The beam time is being used for detector tests and calibration data taking.

(ii) Facility modifications (see Section 3):

(a) During the last year the VERTEX-1 and VERTEX-2 superconducting magnets failed several times mostly due to failures of the cryogenic system. This resulted in a significant loss of beam time and damage of the VERTEX-1 magnet. The severity of the damage and the possibility of its repair will be assessed after a complete warm-up of the magnet, expected at the end of 2015.

(b) The radiation shielding of the H2 beam line was completed in January 2015 before the data taking with primary Ar beams.

(c) Upgrades of the PSD needed for runs with Xe and Pb beams at the top SPS beam momenta were started and will be tested during the 2015 and 2016 Pb beam periods.

(d) New TPC drift velocity chambers needed for the Forward-TPC are developed and tested and will be installed at CERN in spring 2016.

(e) New scintillator beam detectors were manufactured and used during the Ar run. Tests of beam position detectors based on scintillating fibres are ongoing.

(f) The construction of the Forward-TPCs will start soon and the installation is planned in mid-summer 2016.

(g) The status and plans concerning the Vertex Detector are presented in detail in the addendum submitted to the SPSC in parallel to this document [55].

(iii) Software modifications (see Section 4):
The most important achievements associated with the upgrade program of the NA61/SHINE software are:

(a) GEANT4 based NA61/SHINE facility description is fully implemented in the SHINE software including the new detectors,

(b) the SHINE reconstruction chain was validated against the "legacy" chain, validation of the Monte-Carlo chain is in progress,

(c) the Collaboration uses EOS as the main data storage for data analysis,

(d) all services are moved to the CERN cloud infrastructure (CERN OpenStack).

(iv) Numerous new physics results, final and preliminary, were released, see Section 5. They include:

(a) first results on spectra and fluctuations in Ar+Sc collisions,

(b) new results on spectra, fluctuations and correlations in p+p and ^{7}Be+^{9}Be collisions,

(c) new and improved results on cross section and spectra of identified hadrons in p+C interactions at 31 GeV/c,

(d) spectra of charged pions and ρ^0 mesons in π^-+C interactions at 158 and 350 GeV/c.

(v) The data-taking plan for 2016, 2017 and 2018 (see Section 6) includes runs with primary Xe and Pb beams as well as secondary hadron beams needed for measurements for strong interaction and neutrino physics.

(vi) A proposal to extend the NA61/SHINE physics programme (see Section 7) by a beam momentum scan with Pb+Pb collisions is presented in detail in the separate addendum [55] submitted in parallel to this Status Report. Ideas on NA61/SHINE measurements beyond 2020 are briefly summarized and include measurements for strong interactions, neutrino and cosmic ray physics.

Acknowledgments

We would like to thank the CERN PH, BE and EN Departments for the strong support of NA61.

This work was supported by the Hungarian Scientific Research Fund (grants OTKA 68506 and 71989), the János Bolyai Research Scholarship of the Hungarian Academy of Sciences, the Polish Ministry of Science and Higher Education (grants 667/N-CERN/2010/0, NN 202 48 4339 and NN 202 23 1837), the Polish National Science Centre (grants 2011/03/N/ST2/03691, 2012/04/M/ST2/00816 and 2013/11/N/ST2/03879), the Foundation for Polish Science — MPD program, co-financed by the European Union within the European Regional Development Fund, the Federal Agency of Education of the Ministry of Education and Science of the Russian Federation, SPbSU research grant 11.38.193.2014, the Russian Academy of Science and the Russian Foundation for Basic Research (grants 08-02-00018, 09-02-00664 and 12-02-91503-CERN), the Ministry of

Education, Culture, Sports, Science and Technology, Japan, Grant-in-Aid for Scientific Research (grants 18071005, 19034011, 19740162, 20740160 and 20039012), the German Research Foundation (grant GA 1480/2-2), the EU-funded Marie Curie Outgoing Fellowship, Grant PIOF-GA-2013-624803, the Bulgarian Nuclear Regulatory Agency and the Joint Institute for Nuclear Research, Dubna (bilateral contract No. 4418-1-15/17), Ministry of Education and Science of the Republic of Serbia (grant OI171002), Swiss Nationalfonds Foundation (grant 200020117913/1) and ETH Research Grant TH-01 07-3.

References

[1] N. Antoniou *et al.*, [NA61/SHINE Collab.], "Study of hadron production in hadron nucleus and nucleus nucleus collisions at the CERN SPS," 2006. CERN-SPSC-2006-034.

[2] http://www.crystals.saint-gobain.com/uploadedFiles/SG-Crystals/Documents/SGC%20BC418-420-422%20Data%20Sheet.pdf.

[3] http://www2.fisica.unlp.edu.ar/blogs/tgc/XP2020Q-1.pdf.

[4] http://www.hamamatsu.com/resources/pdf/etd/R1828-01_R2059_TPMH1259E04.pdf.

[5] S. Ritt, R. Dinapoli, and U. Hartmann *Nucl. Instrum. Meth.* **A623** (2010) 486. http://www.psi.ch/drs/.

[6] N. Abgrall *et al.*, [NA61/SHINE Collab.] *Eur.Phys.J.* **C74** (2014) 2794, arXiv:1310.2417 [hep-ex].

[7] K. Werner, F.-M. Liu, and T. Pierog *Phys.Rev.* **C74** (2006) 044902.

[8] N. Abgrall, [NA61/SHINE Collaboration Collab.], "Report from the NA61/SHINE experiment at the CERN SPS," Oct, 2014. http://cds.cern.ch/record/1955138.

[9] S. Afanasiev *et al.*, [NA49 Collab.] *Phys. Rev.* **C66** (2002) 054902.

[10] B. Lungwitz, "Phd thesis (2008).". https://edms.cern.ch/document/1237791/1.

[11] K. Grebieszkow for the NA49 Collab. *Nucl. Phys.* **A830** (2009) 547C.

[12] C. Alt *et al.*, [NA49 Collab.] *Phys. Rev.* **C78** (2008) 034914.

[13] V. V. Begun, M. Gazdzicki, M. I. Gorenstein, M. Hauer, V. P. Konchakovski, and B. Lungwitz *Phys. Rev.* **C76** (2007) 024902, arXiv:nucl-th/0611075 [nucl-th].

[14] T. Czopowicz, [NA61/SHINE Collab.] arXiv:1503.01619 [nucl-ex].

[15] A. Bialas, M. Bleszynski, and W. Czyz *Nucl. Phys.* **B111** (1976) 461.

[16] E. Fermi *Prog. Theor. Phys.* **5** (1950) 570–583.

[17] M. Gorenstein and M. Gazdzicki *Phys. Rev.* **C84** (2011) 014904.

[18] V. V. Begun, M. Gazdzicki, and M. I. Gorenstein *Phys. Rev.* **C78** (2008) 024904, arXiv:0804.0075 [hep-ph].

[19] C. Alt *et al.*, [NA49 Collab.] *Phys. Rev.* **C77** (2008) 024903.

[20] C. Alt *et al.*, [NA49 Collab.] *Eur. Phys. J.* **C45** (2006) 343.

[21] A. Aduszkiewicz *et al.*, [NA61/SHINE Collab.] arXiv:1510.00163 [hep-ex].

[22] Z. Koba, H. B. Nielsen, and P. Olesen *Nucl.Phys.* **B40** (1972) 317–334.

[23] M. Gorenstein and M. Rybczynski *Phys.Lett.* **B730** (2014) 70–75, arXiv:1308.0752 [nucl-th].

[24] M. I. Gorenstein and K. Grebieszkow *Phys.Rev.* **C89** no. 3, (2014) 034903, arXiv:1309.7878 [nucl-th].

[25] B. Abelev *et al.*, [ALICE Collab.] *Phys. Rev. Lett.* **110** no. 15, (2013) 152301, arXiv:1207.6068 [nucl-ex].

[26] E. V. Shuryak and M. A. Stephanov *Phys.Rev.* **C63** (2001) 064903, arXiv:hep-ph/0010100 [hep-ph].

[27] S. Bass *et al.* *Prog.Part.Nucl.Phys.* **41** (1998) 255–369, arXiv:nucl-th/9803035 [nucl-th].

[28] M. Bleicher *et al.* *J.Phys.* **G25** (1999) 1859–1896, arXiv:hep-ph/9909407 [hep-ph].

[29] T. Anticic *et al.*, [NA49 Collab.] *Eur. Phys. J.* **C68** (2010) 1–73.

[30] M. Gazdzicki and D. Rohrich *Z.Phys.* **C71** (1996) 55–64, arXiv:hep-ex/9607004 [hep-ex].

[31] M. Gazdzicki and O. Hansen *Nucl.Phys.* **A528** (1991) 754–770.

[32] J. Bachler *et al.*, [NA49 Collaboration Collab.] *Nucl.Phys.* **A661** (1999) 45–54.

[33] F. Verbeure *et al.*, [LEBC-EHS Collab.] *Sov.J.Nucl.Phys.* **54** (1991) 585–611.

[34] A. Rossi, G. Vannini, A. Bussiere, E. Albini, D. D'Alessandro, *et al. Nucl.Phys.* **B84** (1975) 269.

[35] A. Golokhvastov *Phys.Atom.Nucl.* **64** (2001) 1841–1855.

[36] F. Becattini and U. W. Heinz *Z.Phys.* **C76** (1997) 269–286, arXiv:hep-ph/9702274 [hep-ph].

[37] B. B. Back *et al.*, [PHOBOS Collab.] arXiv:nucl-ex/0301017 [nucl-ex].

[38] M. Gazdzicki and D. Roehrich *Z.Phys.* **C65** (1995) 215.

[39] N. Abgrall *et al.*, [NA61/SHINE Collaboration Collab.] *CERN-PH-EP-2015-278 (submitted to EPJ C)* (2015) , arXiv:1510.02703 [hep-ex].

[40] A. Hasler and A. Blondel, "T2K Replica Target Hadron Production Measurements in NA61/SHINE and T2K Neutrino Flux Predictions," 2015. https://cds.cern.ch/record/2039148. Presented 22 Jun 2015.

[41] N. Abgrall *et al.*, [NA61/SHINE Collab.] *Nucl. Instrum. Meth.* **A701** (2013) 99.

[42] T. Adye *Proceedings of the PHYSTAT 2011 Workshop on Statistical Issues Related to Discovery Claims in Search Experiments and Unfolding, CERN, Geneva, Switzerland, CERN-2011-006* (2011) 313–318. http://hepunx.rl.ac.uk/~adye/software/unfold/RooUnfold.html.

[43] G. D'Agostini *Nucl. Instrum. Meth.* **A 362** (1995) 487–498.

[44] A. Herve for the NA61/SHINE Coll. *to appear in Proc. 34th ICRC* (2015) .

[45] G. I. Veres, *Baryon Momentum Transfer in Hadronic and Nuclear Collisions at the CERN NA49 Experiment*. PhD thesis, Eötvös Loránd University, Budapest, 2001.

[46] T. Pierog, I. Karpenko, J. M. Katzy, E. Yatsenko, and K. Werner *Phys. Rev.* **C92** no. 3, (2015) 034906, arXiv:1306.0121 [hep-ph].

[47] E.-J. Ahn, R. Engel, T. K. Gaisser, P. Lipari, and T. Stanev *Phys.Rev.* **D80** (2009) 094003, arXiv:0906.4113 [hep-ph].

[48] S. Ostapchenko *Phys.Rev.* **D83** (2011) 014018, arXiv:1010.1869 [hep-ph].

[49] S. Roesler, R. Engel, and J. Ranft, "The Monte Carlo event generator DPMJET-III," in *Proc. MC2000*, pp. 1033–1038. 2000. arXiv:hep-ph/0012252 [hep-ph].

[50] H.-J. Drescher *Phys.Rev.* **D77** (2008) 056003, arXiv:0712.1517 [hep-ph].

[51] T. Pierog and K. Werner *Phys. Rev. Lett.* **101** (2008) 171101, arXiv:astro-ph/0611311 [astro-ph].

[52] https://web.ikp.kit.edu/rulrich/crmc.html.

[53] N. Agababyan *et al.*, [EHS-NA22 Collaboration Collab.] *Z.Phys.* **C46** (1990) 387–395.

[54] N. Abgrall *et al.*, [NA61/SHINE Collab.], "NA61/SHINE plans beyond the approved program," 2012. CERN-SPSC-2012-022; SPSC-P-330-ADD-6.

[55] A. Aduszkiewicz *et al.*, [NA61/SHINE Collab.], "Beam momentum scan with Pb+Pb collisions at the CERN SPS," 2015. Addendum to the NA61/SHINE proposal submitted to the SPSC on October 14, 2015.